

# Exploring the effect of different cosmologies on the Epoch of Reionization 21-cm signal with POLAR

Anshuman Acharya<sup>1\*</sup>, Qing-bo Ma<sup>2,3</sup>, Sambit K. Giri<sup>4</sup>, Benedetta Ciardi<sup>1</sup>, Raghunath Ghara<sup>5</sup>, Garrelt Mellema<sup>6</sup>, Saleem Zaroubi<sup>7,8</sup>, Ian Hothi<sup>9,10</sup>, Ilian T. Iliev<sup>11</sup>, Léon V. E. Koopmans<sup>7</sup>, Michele Bianco<sup>12</sup>

<sup>1</sup>Max-Planck-Institut für Astrophysik, Garching 85748, Germany

<sup>2</sup>School of Physics and Electronic Science, Guizhou Normal University, Guiyang 550001, PR China

<sup>3</sup>Guizhou Provincial Key Laboratory of Radio Astronomy and Data Processing, Guizhou Normal University, Guiyang 550001, PR China

<sup>4</sup>Nordita, KTH Royal Institute of Technology and Stockholm University, Hannes Alfvéns väg 12, SE-106 91 Stockholm, Sweden

<sup>5</sup>Department of Physical Sciences, Indian Institute of Science Education and Research Kolkata, Mohanpur, WB 741 246, India

<sup>6</sup>The Oskar Klein Centre, Department of Astronomy, Stockholm University, AlbaNova, SE-10691 Stockholm, Sweden

<sup>7</sup>Kapteyn Astronomical Institute, University of Groningen, P.O. Box 800, 9700AV Groningen, The Netherlands

<sup>8</sup>Astrophysics Research Centre of the Open University of Israel, Ra'anana 4353701, Israel

<sup>9</sup>LERMA, Observatoire de Paris, PSL Research University, CNRS, Sorbonne Université, F-75014 Paris, France

<sup>10</sup>Laboratoire de Physique de l'ENS, ENS, Université PSL, CNRS, Sorbonne Université, Université Paris Cité, 75005, Paris, France

<sup>11</sup>Astronomy Centre, Department of Physics & Astronomy, Pevensey III Building, University of Sussex, Falmer, Brighton, BN1 9QH, United Kingdom

<sup>12</sup>Institute for Particle Physics and Astrophysics, ETH Zurich, Wolfgang-Pauli-Str 27, 8093 Zurich, Switzerland

Accepted XXX. Received YYY; in original form ZZZ. NORDITA-2024-035

## ABSTRACT

A detection of the 21-cm signal power spectrum from the Epoch of Reionization is imminent, thanks to consistent advancements from telescopes such as LOFAR, MWA, and HERA, along with the development of SKA. In light of this progress, it is crucial to expand the parameter space of simulations used to infer astrophysical properties from this signal. In this work, we explore the role of cosmological parameters such as the Hubble constant  $H_0$  and the matter clustering amplitude  $\sigma_8$ , whose values as provided by measurements at different redshifts are in tension. We run  $N$ -body simulations using GADGET-4, and post-process them with the reionization simulation code POLAR, that uses L-GALAXIES to include galaxy formation and evolution properties and GRIZZLY to execute 1-D radiative transfer of ionizing photons in the intergalactic medium (IGM). We compare our results with the latest JWST observations and explore which astrophysical properties for different cosmologies are necessary to match the observed UV luminosity functions at redshifts  $z = 10$  and  $9$ . Additionally, we explore the impact of these parameters on the observed 21-cm signal power spectrum, focusing on the redshifts within the range of LOFAR 21-cm signal observations ( $z \approx 8.5 - 10$ ). Despite differences in cosmological and astrophysical parameters, the 21-cm power spectrum at these redshifts agrees with presently observed upper limits. This suggests the need for broader physical parameter spaces for inference modeling to account for all models that agree with observations. However, we also propose stronger constraining power by using a combination of galactic and IGM observables.

**Key words:** cosmology: dark ages, reionization, first stars; cosmology: theory; galaxies: formation;

## 1 INTRODUCTION

The Epoch of Reionization (EoR) refers to the period of the Universe when sufficient astrophysical objects formed and emitted UV photons to (re)ionize the neutral hydrogen of the intergalactic medium (IGM). One of the most important probes for studying this epoch is the brightness temperature fluctuations of the 21-cm line of neutral hydrogen (HI) as observed in emission or absorption against the Cosmic Microwave Background radiation (CMB; Field 1959; Hogan & Rees 1979; Madau et al. 1997; Shaver et al. 1999; Tozzi et al. 2000; Ciardi & Madau 2003; Zaroubi 2013). The 21-cm signal is produced

by the forbidden hyperfine spin-flip transition of the ground state of neutral hydrogen. As the excited state has an extremely long lifetime and neutral hydrogen is abundant in the IGM at the start of the EoR, this signal can be used as a tracer of the IGM ionization state. A statistical detection of the strength of the fluctuations of its brightness temperature allows us to constrain models of the Universe during this early formation stage.

\* E-mail: anshuman@mpa-garching.mpg.de

For this purpose, multiple interferometric low-frequency radio

telescopes have been designed, such as PAPER<sup>1</sup>, MWA<sup>2</sup>, HERA<sup>3</sup>, LOFAR<sup>4</sup>, and the upcoming SKA<sup>5</sup>. While the signal is yet to be detected, upper limits of the 21-cm power spectrum have been obtained and are becoming increasingly tighter (e.g., Mertens et al. 2020; Trott et al. 2020; HERA Collaboration et al. 2023; Acharya et al. 2024c). These have allowed us to rule out some extreme astrophysical models through comparisons with simulations (e.g., Ghara et al. 2020; Mondal et al. 2020; Greig et al. 2021a,b; Abdurashidova et al. 2022). New methods that utilize multi-redshift power spectrum observations (Ghara et al. 2024; Choudhury et al. 2024), wavelet statistics (Hothi et al. 2024), and simulation-based inference (Saxena et al. 2023; Greig et al. 2024) have also been developed to improve the understanding of parameters governing the properties of the IGM.

At the same time, galaxies that formed during the EoR that are responsible for HI ionization have also been studied using hydrodynamical and/or radiative transfer simulations with different prescriptions, such as CROC (Gnedin 2014; Gnedin & Kaurov 2014; Esmerian & Gnedin 2021, 2022, 2024), FIRE (Ma et al. 2018), TECHNICAL DAWN (Finlator et al. 2018), SPHINX (Rosdahl et al. 2018), CRASH simulations (Eide et al. 2018, 2020; Ma et al. 2021; Kostyuk et al. 2023; Basu et al. 2024), C<sup>2</sup>RAY simulations (Mellema et al. 2006; Dixon et al. 2016; Giri & Mellema 2021; Hirling et al. 2024; Giri et al. 2024), CoDA I,II, III (Ocvirk et al. 2016, 2020; Lewis et al. 2022), ASTRID (Bird et al. 2022), COLDSIM (Maio et al. 2022; Casavecchia et al. 2024), THESAN (Kannan et al. 2022; Garaldi et al. 2022; Smith et al. 2022; Garaldi et al. 2024), and SPICE (Bhagwat et al. 2024). Although these simulations are ideal tools to investigate the IGM and galactic properties, they are computationally expensive and thus limited in box size and/or in the number of simulations that can be run. Thus, they cannot be used for building a wide range of models for comparison with the 21-cm power spectrum or their upper limits.

To this aim, semi-numerical approaches such as SIMFAST21 (Santos et al. 2010a,b), BEARS (Thomas et al. 2009), 21cmFAST (Mesinger & Furlanetto 2007; Mesinger et al. 2011), GRIZZLY (Ghara et al. 2015, 2018), REIONYUGA (Mondal et al. 2017), ARTIST (Molaro et al. 2019), AMBER (Trac et al. 2022) and BEORN (Schaeffer et al. 2023) are typically employed. To incorporate a more realistic modeling of galactic properties into these methods, codes such as ASTRAEUS (Hutter et al. 2021, 2024), MERAXES (Mutch et al. 2016; Balu et al. 2023) and POLAR (Ma et al. 2023, hereafter M23) have been developed.

The LOFAR EoR Key Science Project (KSP) team has designed POLAR, a semi-numeric approach which strikes a balance between speed and complexity of relevant physical processes, by post-processing  $N$ -body Dark Matter (DM) simulations with Semi-Analytic Models (SAMs) of galaxy formation and evolution, and subsequently applying the 1D radiative transfer (RT) code GRIZZLY (Ghara et al. 2015, 2018), an updated version of BEARS (Thomas et al. 2009). This allows a fast modeling of the 21-cm signal power spectrum, while at the same time accounting for important galactic properties and RT effects. Consequently, observations of the 21-cm line can also be combined with data obtained in other frequency bands (e.g. from JWST) to jointly constrain IGM and galactic properties.

Here, we investigate the impact of varying cosmological param-

eters on the 21-cm signal at  $z \approx 10.11, 9.16$ , and  $8.3$ , i.e. the three redshifts targeted by LOFAR (Mertens et al. 2024, in prep). We focus on those parameters whose low and high redshift measurements are in tension, i.e., the Hubble parameter  $H_0 = 100h \text{ km s}^{-1} \text{ Mpc}^{-1}$  and the matter clustering amplitude  $\sigma_8$ . Our fiducial model is the one of Planck Collaboration et al. (2020), with  $h = 0.6766$  and  $\sigma_8 = 0.8102$ , while a higher  $h$  value is adopted to explore the low redshift measurement of  $h = 0.733$  from studies of Cepheid variables in the host galaxies of 42 Type Ia supernovae (Riess et al. 2022). Similarly, a lower  $\sigma_8$  value of  $0.702$  is adopted from the low redshift measurement of anisotropic galaxy clustering measurement analysis (Tröster et al. 2020). Lastly, we also adopt a  $\sigma_8 = 0.88$  from recent eROSITA results (Ghirardini et al. 2024) to consider both extremes of  $\sigma_8$  measurements. Motivated by results obtained in the context of the 21-cm signal shown by Giri et al. (2023) and Acharya et al. (2024b), we additionally implement the Fixed & Paired (F&P) approach (Angulo & Pontzen 2016) to boost effective volumes of the simulations and suppress cosmic variance.

The paper is structured as follows. In Section 2, we discuss the setup of the POLAR simulations with different cosmologies. In Section 3 we present the resulting galactic and IGM properties, and in Section 4 we discuss the implications of varying astrophysical and cosmological parameters for inference modeling from 21-cm signal observations, jointly constrained with other observables of the EoR. Finally, we summarize our results in Section 5.

## 2 METHODOLOGY

Building on M23, we utilize a similar setup by running  $N$ -body DM simulations, and then post-processing them with the L-GALAXIES SAM (Barrera et al. 2023; Henriques et al. 2015, 2020) to model the formation and evolution of galaxies, and with the 1D radiative transfer code GRIZZLY (Ghara et al. 2015, 2018) to model the gas ionization and the 21-cm signal from neutral hydrogen. In Sections 2.1 and 2.2, we highlight the key parameters used for setting up the simulations and the analysis done in this work. Further, in Section 2.3 we propose two cases: one where we keep the astrophysical parameters the same for all four cosmological models, and one in which we tune them to match UV luminosity functions (UVLFs) observed with JWST and HST at  $z = 10$  and  $9$ . We refer to the first and second case as “unconstrained” and “constrained”, respectively.

### 2.1 Dark-matter simulations

We use the GADGET-4 code (Springel et al. 2021) for running  $N$ -body DM simulations with a volume of  $(150h^{-1} \text{ cMpc})^3$  and  $2048^3$  DM particles. This translates into a DM particle mass of  $5 \times 10^7 M_\odot$ , matching the particle resolution of larger simulations used by the LOFAR EoR KSP team (see for example Giri et al. 2019b,a). The box size is chosen to probe wave-modes of  $k \leq 1.0h \text{ cMpc}^{-1}$ , where the best results from observations with LOFAR, HERA, MWA (and eventually SKA) are expected (Koopmans et al. 2015). This condition requires simulations with box sizes  $> 100h^{-1} \text{ cMpc}$  (Iliev et al. 2014), although Kaur et al. (2020) suggests box sizes  $> 175h^{-1} \text{ cMpc}$  being necessary when accounting for X-ray heating of the IGM. To sidestep this issue, we assume that at our redshifts of interest, the IGM has already been heated above the CMB temperature (see Section 2.2.2). We additionally employ the F&P approach (Angulo & Pontzen 2016) to mitigate sample variance, and thus run two realisations of each DM simulation. Each pair of realisations has the mode amplitudes fixed to the square root of the initial matter power

<sup>1</sup> Precision Array to Probe EoR, <http://eor.berkeley.edu>

<sup>2</sup> Murchison Widefield Array, <http://www.mwatelescope.org>

<sup>3</sup> Hydrogen Epoch of Reionization Array, <https://reionization.org/>

<sup>4</sup> Low-Frequency Array, <http://www.lofar.org>

<sup>5</sup> Square Kilometre Array, <https://www.skao.int/en>

**Table 1.** The four  $N$ -body dark matter simulation models considered in this work. From left to right, the model name, the adopted value of  $h$  and  $\sigma_8$ , and the reference for the values. All other cosmological parameters are fixed to the Planck Collaboration et al. (2020) values.

Model	$h$	$\sigma_8$	Reference
fiducial	0.6766	0.8102	Planck Collaboration et al. (2020)
$h$ high	0.7330	0.8102	Riess et al. (2022)
$\sigma_8$ low	0.6766	0.7020	Tröster et al. (2020)
$\sigma_8$ high	0.6766	0.8800	Ghirardini et al. (2024)

spectrum, and the phases of the second realisations (B-series) are obtained by mirroring those of the first realisations (A-series). The F&P approach of averaging observables of these two realisations has been shown to boost the statistical precision of the matter power spectrum, bispectrum and halo mass function (Angulo & Pontzen 2016; Chartier et al. 2021; Maion et al. 2022; Villaescusa-Navarro et al. 2018), Lyman- $\alpha$  power spectra (Anderson et al. 2019), 21-cm signal power spectrum and bispectrum (Giri et al. 2023; Acharya et al. 2024b) and several other quantities derived from simulations (Villaescusa-Navarro et al. 2018; Klypin et al. 2020). Beyond this, we use the same random seed to minimize the effect of randomized initial conditions for both the A and B-series of simulations.

For our reference simulation, we assume a “fiducial”  $\Lambda$ -Cold Dark Matter ( $\Lambda$ CDM) cosmological model based on Planck Collaboration et al. (2020, specifically the TT,TE,EE+lowE+lensing+BAO case), setting  $\Omega_\Lambda = 0.6889$ ,  $\Omega_m = \Omega_b + \Omega_{dm} = 0.3111$ ,  $\Omega_b = 0.04897$ ,  $H_0 = 100h \text{ km s}^{-1} \text{ Mpc}^{-1}$  with  $h = 0.6766$ ,  $\sigma_8 = 0.8102$  and  $n_s = 0.9665$ , where the symbols have their usual meaning. Further, we consider three additional cosmologies, where we vary  $h$  and  $\sigma_8$ , while keeping the other parameters fixed to the above-mentioned values. This is necessary to consider the maximum impact of changing cosmological parameters across the range of observed values. First, we adopt  $h = 0.7330$  (from Riess et al. 2022), and refer to this as the “ $h$  high” model. In addition, we explore two extreme values of  $\sigma_8$ , namely the “ $\sigma_8$  low” case with  $\sigma_8 = 0.702$  (Tröster et al. 2020), and the “ $\sigma_8$  high” case with  $\sigma_8 = 0.88$  (Ghirardini et al. 2024). The details of the four simulation models are listed in Table 1.

The initial conditions for all simulations are generated at  $z = 199$  with a second-order Lagrangian perturbation theory based on the NGENIC algorithm implemented into GADGET-4, using the same linear theory power spectrum as Hernández-Aguayo et al. (2023). We generate 90 snapshots between  $z = 20$  and  $z = 5$ , for which we save full snapshot information. However, in order to ensure a maximum step size of 10 Myrs between snapshots used to build halo merger trees with the Friend-Of-Friends (FOF) group finding algorithm (Springel et al. 2001), we perform a finer gridding to generate a total of 156 output time steps for FOF groups. We use a standard linking length of 0.2 times the mean particle spacing and a minimum group size of 64 DM particles (corresponding to a minimum halo size of  $\approx 3 \times 10^9 M_\odot$ ). Substructures within halos are identified using the SUBFIND-HBT algorithm (Han et al. 2018; Springel et al. 2021). Finally, the gravitational softening length is set to 0.025 of the mean particle spacing, i.e.  $\approx 1.83h^{-1} \text{ ckpc}$ .

To evaluate the performance of the simulations, in Figure 1 we present the halo mass function (HMF) as  $M_h \frac{dn_h}{dM_h}$ , where  $M_h$  and  $n_h$  are the halo mass and number density respectively, and compare them with fits by Tinker et al. (2008), computed using the Python package HMF (Murray 2014) at  $z = 9$  and 10. As in this study, Tinker et al. (2008) takes into account the non-universality of the HMF by considering the impact of varying the cosmological parameters

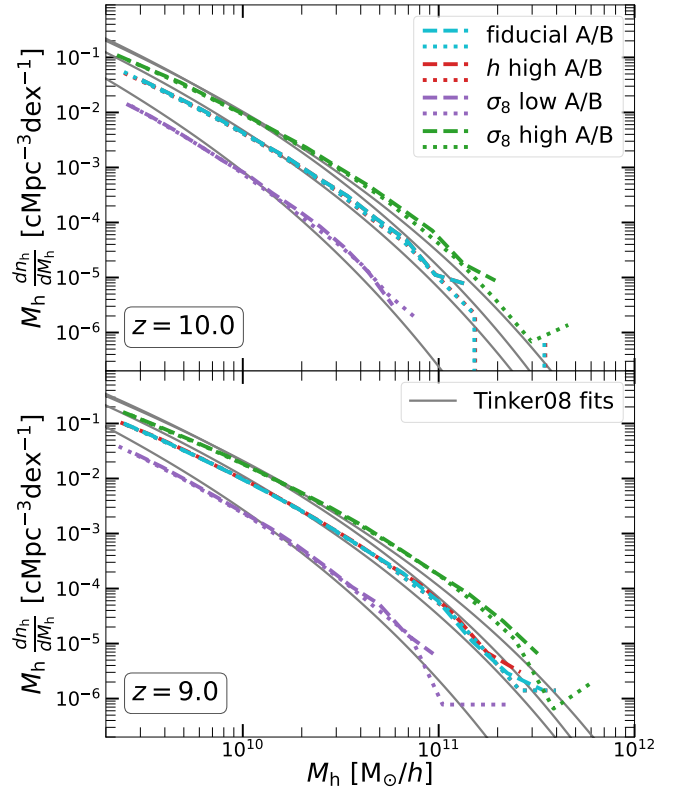


**Figure 1.** Halo mass functions for our four models: fiducial (cyan),  $h$  high (red),  $\sigma_8$  low (purple) and  $\sigma_8$  high (green) at  $z = 10$  (top panel) and 9 (bottom). The A- and B-series are shown with dashed and dotted lines, respectively. The corresponding fit for each simulation using the Tinker et al. (2008) model is shown with a solid grey line.

in the  $\Lambda$ CDM model. We note that the fiducial and  $h$  high models at these redshifts produce very similar HMFs, despite some noticeable differences in their corresponding fits. A deeper exploration indicates that our simulation setup is less sensitive to differences in the Hubble parameter, given the choice of the starting redshift, and that the initial conditions were generated using second-order Lagrangian perturbation theory. A significantly higher starting redshift or third/fourth-order Lagrangian perturbation theory may thus be required to better match the fits. Nevertheless, some differences do exist, especially at the extremities of the HMF, which lead to the differences noted in the subsequent sections.

Further, we also find a mild under-prediction of the HMF at the low mass end and an over-prediction at the high mass end. This may be due to the choice of the linking length of 0.2, which at significantly high redshifts may lead to overlinking. A lower value of 0.17, as suggested by Watson et al. (2013), may resolve this issue. However, we still use 0.2 for minimizing differences between the setups used for past applications of L-GALAXIES (e.g., Henriques et al. 2015, 2020; Barrera et al. 2023, and M23) and our setup. Lastly, we note that the B-series has slightly more massive halos in all models. This is purely because of the choice of the random seed, which happens to lead to some regions of massive halo formation in the B-series where the A-series have voids.

## 2.2 Galactic and IGM properties with POLAR

POLAR is a semi-numerical model designed to obtain high- $z$  galaxy properties and the 21-cm signal from the IGM in a fast and robust

manner. It combines the semi-analytical galaxy formation and evolution model of L-GALAXIES (Henriques et al. 2015, 2020; Barrera et al. 2023) with the one-dimensional radiative transfer code GRIZZLY (Ghara et al. 2015, 2018).

### 2.2.1 Semi-Analytic modeling of galaxies

We use L-GALAXIES as described by Barrera et al. (2023), as a post-processing module of GADGET-4. This is an updated version of the publicly available L-GALAXIES 2020 that was used by M23. L-GALAXIES implements most major physical processes of gas cooling, star formation, galaxy mergers, supernovae feedback, black hole growth, AGN feedback, and dust attenuation. While Barrera et al. (2023) largely builds on Henriques et al. (2015), we also consider the parameters used by Henriques et al. (2020) before adapting them for our purposes. In particular, we focus on those that control star formation efficiency ( $\alpha_{\text{SF}}$ ), star formation efficiency during galaxy mergers ( $\alpha_{\text{SF,burst}}$ ), AGN accretion rate ( $k_{\text{AGN}}$ ), reheating of cold gas by star formation ( $\epsilon_{\text{reheat}}$ ,  $V_{\text{reheat}}$ ), and the energy released by each supernova ( $E_{\text{SN}}$ ).

We tune the parameters to match photometric observations of the UVLFs from JWST and HST at  $z = 10$  and  $9$ , as these redshifts are observationally relevant for the LOFAR EoR KSP. We note that L-GALAXIES assumes a 100% escape fraction for the UV photons, and thus we also implement the dust attenuation approach of Henriques et al. (2015). However, this is a simplified model and more complex ones may lead to greater suppression of the UV luminosity function. In Table 2 we list all the possible parameters available in L-GALAXIES, and their values set to match UVLF observations as discussed in Section 2.3.

### 2.2.2 Radiative transfer and the 21-cm signal

Modeling the EoR requires the inclusion of radiative transfer to describe the hydrogen ionization and heating. For this, we take the results of the  $N$ -body simulations from Section 2.1 and the semi-analytic modeling of galaxies from Section 2.2.1, and post-process them with the 1D radiative transfer code GRIZZLY, as done by M23. GRIZZLY uses pre-computed ionization and temperature profiles of gas for different source and density properties at various redshifts to model the ionization and heating processes and the differential brightness temperature of the 21-cm signal ( $\delta T_{\text{b}}$ ).

More specifically, GRIZZLY requires as input the gridded matter density field and dark matter halo masses from the  $N$ -body simulation, as well as the corresponding galactic stellar masses and stellar ages obtained with L-GALAXIES. Our reference simulation has a grid of  $256^3$  cells, resulting in a cell size of  $\approx 600 h^{-1}$  ckpc, but we use a range of different sizes (from  $64^3$  to  $512^3$  cells) to assure convergence of output values in the range  $12 > z > 5$ . Next, we assume that the gas density scales by a factor of  $\Omega_{\text{b}}/\Omega_{\text{dm}}$  with the dark matter density. Lastly, as done in M23, we use the Binary Population and Spectral Synthesis (BPASS; Stanway & Eldridge 2018) code to model the Spectral Energy Distributions (SEDs) of stellar sources. In future work, we will also explore the impact of other source types such as X-ray binaries, shock-heated interstellar medium, and accreting black holes (as done in Eide et al. 2018, 2020; Ma et al. 2021).

GRIZZLY computes  $\delta T_{\text{b}}$  as follows (see Furlanetto et al. 2006):

$$\delta T_{\text{b}} = 27x_{\text{HI}}(1 + \delta_{\text{B}}) \left( 1 - \frac{T_{\text{CMB}}}{T_{\text{S}}} \right) \times \left[ \left( \frac{\Omega_{\text{b}} h^2}{0.023} \right) \left( \frac{0.15}{\Omega_{\text{m}} h^2} \frac{1+z}{10} \right)^{1/2} \right] \text{mK}, \quad (1)$$

where  $x_{\text{HI}}$  is the fraction of neutral hydrogen,  $\delta_{\text{B}}$  is the fractional overdensity of baryons,  $T_{\text{S}}$  is the hydrogen spin temperature,  $T_{\text{CMB}}$  is the temperature of the CMB photons at redshift  $z$ , and  $\Omega_{\text{m}}$  is the total matter density. As done by M23, we assume  $T_{\text{S}} \gg T_{\text{CMB}}$  which is valid when the IGM has been sufficiently heated by X-ray sources and expected to be the case in the range of redshift of interest here. Additionally, we also ignore the impact of redshift space distortions. Thus Equation 1 is reduced to

$$\delta T_{\text{b}} = 27x_{\text{HI}}(1 + \delta_{\text{B}}) \left[ \left( \frac{\Omega_{\text{b}} h^2}{0.023} \right) \left( \frac{0.15}{\Omega_{\text{m}} h^2} \frac{1+z}{10} \right)^{1/2} \right] \text{mK}. \quad (2)$$

We define the power spectrum of  $\delta T_{\text{b}}$  as:

$$P_{21\text{cm}}(\mathbf{k}) = \delta_{\text{D}}(\mathbf{k} + \mathbf{k}') \langle \delta T_{\text{b}}(\mathbf{k}) \delta T_{\text{b}}(\mathbf{k}') \rangle, \quad (3)$$

where  $\delta_{\text{D}}$  is the Dirac delta function,  $\delta T_{\text{b}}(\mathbf{k})$  is the differential brightness temperature in Fourier space, and  $\langle \dots \rangle$  is the ensemble average. In the following, we will report our results in terms of the normalized form of the power spectrum, given by (see Peacock 1999, for details):

$$\Delta_{21\text{cm}}^2(k) = \frac{k^3}{2\pi^2} \times P_{21\text{cm}}(k). \quad (4)$$

## 2.3 UV luminosity functions

Because Henriques et al. (2015, 2020) tuned the L-GALAXIES parameters to the low-redshift Universe ( $z < 3$ ), it is necessary to adapt them to match the redshift regime that we are interested in (see Vani et al. 2024, on discrepancies from observations at higher redshifts). In particular, for the LOFAR EoR KSP team, focussing on  $10 > z > 8.5$  is crucial, as this is the regime in which the LOFAR telescope is most sensitive. Thus, we change the values of the parameters listed in Section 2.2.1 to match the observations of the UVLFs from HST legacy fields and JWST programs (Finkelstein et al. 2015; Bouwens et al. 2015, 2021; Harikane et al. 2022; Bouwens et al. 2023a,b; Harikane et al. 2023; Leung et al. 2023; McLeod et al. 2024; Adams et al. 2024) at  $z = 10$  and  $9$ . We have also varied other parameters, but their impact on the UVLFs is minimal (see M23, for a detailed analysis of the impact of different parameters). In future work, we will broaden the range of astrophysical parameters and analyse their effect on other observables.

First, we tune the  $\alpha_{\text{SF}}$ ,  $\alpha_{\text{SF,burst}}$ , and  $E_{\text{SN}}$  values in order for the fiducial case to match the observed high- $z$  UVLFs. Additionally, we reduce the value of the fraction of AGN formed ( $k_{\text{AGN}}$ ) by a small amount, which improves the agreement at the brightest magnitudes ( $M_{1600,\text{AB}} < -20$ ). Similarly, the supernova feedback-based heating efficiency parameters  $\epsilon_{\text{reheat}}$  and  $V_{\text{reheat}}$  are changed to improve the agreement for  $M_{1600,\text{AB}} > -19$ .

We consider two more cases. In the first one, the same L-GALAXIES parameters of the fiducial model above are adopted for all  $N$ -body simulations, to investigate the impact of different cosmologies on the 21-cm signal independently from observations of galaxies at high redshifts. We refer to this model as ‘‘unconstrained’’. This case allows us to have a clearer picture of the impact of changing cosmologies on the 21-cm signal, without astrophysical processes potentially cancelling out their effects on observables. In the second

**Table 2.** List of astrophysical parameters in L-GALAXIES (see Henriques et al. 2015, 2020, for more details) that can be tuned to control galaxy formation and evolution. We show the names of the parameters in column 1, and Henriques et al. (2015) and Henriques et al. (2020) values tuned to  $z < 3$  observations in columns 2 and 3. Our cosmological models (fiducial,  $h$  high,  $\sigma_8$  low and  $\sigma_8$  high) tuned to UVLF observations at  $z = 10$  and 9 are shown in columns 4, 5, 6 and 7 respectively. We highlight the parameters that differ from Henriques et al. (2015, 2020) values in bold. For the unconstrained case (see text for more details), we use the fiducial model parameters for all our  $N$ -body simulations.

Parameter	Henriques et al. (2015)	Henriques et al. (2020)	fiducial	$h$ high	$\sigma_8$ low	$\sigma_8$ high
$\alpha_{\text{SF}}$	0.025	0.060	<b>0.20</b>	<b>0.20</b>	<b>0.50</b>	<b>0.20</b>
$\alpha_{\text{SF,burst}}$	0.60	0.50	<b>0.80</b>	<b>0.80</b>	<b>0.90</b>	<b>0.80</b>
$\beta_{\text{SF,burst}}$	1.90	0.38	0.38	0.38	0.38	0.38
$k_{\text{AGN}} [10^{-3}M_{\odot} \text{ yr}^{-1}]$	5.3	2.5	<b>2.0</b>	<b>2.0</b>	<b>2.0</b>	<b>2.0</b>
$f_{\text{BH}}$	0.041	0.066	0.066	0.066	0.066	0.066
$V_{\text{BH}} [\text{km s}^{-1}]$	750	700	700	700	700	700
$M_{\text{r.p.}} [10^{14}M_{\odot}]$	1.2	5.1	5.1	5.1	5.1	5.1
$\alpha_{\text{dyn.fric.}}$	2.5	1.8	1.8	1.8	1.8	1.8
$\epsilon_{\text{reheat}}$	2.6	5.6	<b>8.0</b>	<b>8.0</b>	<b>8.0</b>	<b>8.0</b>
$V_{\text{reheat}} [\text{km s}^{-1}]$	480	110	<b>250</b>	<b>250</b>	<b>250</b>	<b>250</b>
$\beta_{\text{reheat}}$	0.72	2.90	2.90	2.90	2.90	2.90
$\eta_{\text{eject}}$	0.62	5.50	5.50	5.50	5.50	5.50
$V_{\text{eject}} [\text{km s}^{-1}]$	100	220	220	220	220	220
$\beta_{\text{eject}}$	0.8	2.0	2.0	2.0	2.0	2.0
$\gamma_{\text{reinc}} [10^{10} \text{ yr}^{-1}]$	3.0	1.2	1.2	1.2	1.2	1.2
$E_{\text{SN}} [10^{51} \text{ erg}]$	1.0	1.0	<b>0.80</b>	1.0	<b>0.15</b>	<b>2.00</b>
$Z_{\text{yield}}$	0.030	0.030	0.030	0.030	0.030	0.030

case, called ‘‘constrained’’, the L-GALAXIES parameters (specifically  $\alpha_{\text{SF}}$ ,  $\alpha_{\text{SF,burst}}$ , and  $E_{\text{SN}}$ ) are changed for each cosmological model to match the observed UVLFs. This is potentially more interesting, as it allows for a joint constraint of astrophysical and cosmological parameters based on multi-frequency observations. The L-GALAXIES parameters adopted are listed in Table 2.

We show the UVLFs for the unconstrained (top) and constrained case (bottom) in Figure 2 for all cosmological models, along with observations at  $z = 10$  and 9. In the unconstrained case, we note that the fiducial and  $h$  high models have similar UVLFs, while the  $\sigma_8$  low model underpredicts the UVLF as compared to observations. On the other hand, the UVLF in the  $\sigma_8$  high model is mildly overpredicted. These results are in agreement with the impact that these parameters are expected to have on matter clustering. In the constrained case, the boost in star formation due to higher  $\alpha_{\text{SF}}$  and  $\alpha_{\text{SF,burst}}$  values and a lower  $E_{\text{SN}}$  value, allows the  $\sigma_8$  low model to match the bright end of the UVLF. However, due to lower matter clustering, it does not produce as many faint galaxies as the other cases, and sees a steep drop at  $M_{1600,\text{AB}} > -18$ . On the other hand, the high  $E_{\text{SN}}$  in the  $\sigma_8$  high model strongly suppresses star formation and thus matches other cosmological models, as well as JWST and HST observations. Additionally, it produces more faint galaxies even at  $M_{1600,\text{AB}} > -16$ . Between the  $h$  high and fiducial models, the difference is minimal at  $z = 10$  due to the mildly higher  $E_{\text{SN}}$  in the  $h$  high model. However, at  $z = 9$  the impact of higher matter clustering in the  $h$  high model shows up in the form of more galaxies at the low luminosity end.

Lastly, we note that in the fiducial model the brightest galaxy at  $z = 14$  has  $M_{1600,\text{AB}} = -20.36$ , while at  $z = 13$  it has  $M_{1600,\text{AB}} = -20.60$ , which is in agreement with the recent spectroscopically confirmed galaxies at  $z = 14.32$  and  $13.90$  (Carniani et al. 2024). For completeness, in Appendix A we also show the UVLFs in the range  $12 > z > 5$  for the constrained case. We find that our models reasonably agree with UVLF observations across this redshift range.

## 2.4 Reionization history

Before discussing the reionization history in more detail, we note that the escape fraction of UV photons had been set to  $f_{\text{esc}} = 12.5\%$  in order for the fiducial model to reionize completely (i.e. the average neutral fraction  $\langle x_{\text{HI}} \rangle$  becomes zero) by  $z = 5$ . For the other models, though, full reionization is reached at different redshifts. In the future we plan to consider  $f_{\text{esc}}$  as a free parameter as well, although, as a reference, in Appendix C we show the reionization history of the fiducial model with  $f_{\text{esc}} = 25\%$ .

For a qualitative view of the reionization history, in Figure 3 we show the A-series (i.e. with ‘‘fixed’’ initial conditions in the F&P pair of simulations) middle slices of the  $\delta T_{\text{b}}$  cubes for the four cosmological models in the constrained case at  $z = 12, 10, 8$  and 6. We note that there are no major differences until  $z = 8$ , when more and larger ionized regions appear in the  $\sigma_8$  low model, while less and smaller ones are present in the  $\sigma_8$  high model. This leads to the  $\sigma_8$  low model being completely ionized by  $z = 6$ , while the  $\sigma_8$  high model still has large neutral regions. This is because, contrary to the fiducial model, in these cases the choice of the parameters controlling the astrophysical processes has an impact stronger than the one of  $\sigma_8$  on the matter clustering. However, the differences between the astrophysical parameters of the  $h$  high and the fiducial model are smaller, so that the differences in the size of the ionized regions from  $z = 10$  is mainly driven by matter clustering. Nevertheless, the choice of both astrophysical and cosmological parameters leads to significantly different speeds at which reionization happens across all four models. Indeed, despite the relatively similar maps observed at  $z = 8$ , by  $z = 6$  the differences are much more evident. For completeness, in Appendix B we also show the B-series middle slices.

In Figure 4, we present the redshift evolution of the average of the A and B-series volume-averaged neutral hydrogen fraction,  $\langle x_{\text{HI}} \rangle$ , in the unconstrained (top) and constrained (bottom) cases, together with observational constraints. As in some models the redshift of reionization is not properly captured due to the coarse redshift reso-

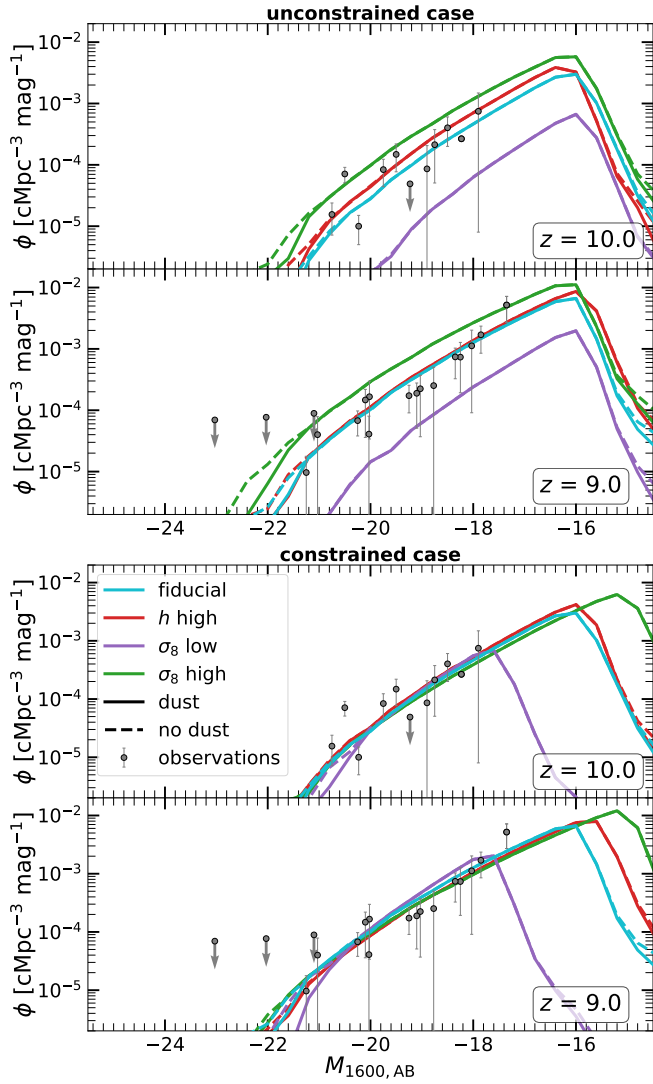


**Figure 2.** A and B-series averaged UVLFs for the unconstrained (top) and constrained (bottom) cases at  $z = 10$  and  $9$  for the fiducial (cyan),  $h$  high (red),  $\sigma_8$  low (purple) and  $\sigma_8$  high (green). We also show the dust attenuated (solid) and unattenuated (dashed) UVLFs, and JWST and HST observations (Finkelstein et al. 2015; Bouwens et al. 2015, 2021; Harikane et al. 2022; Bouwens et al. 2023a,b; Harikane et al. 2023; Leung et al. 2023; McLeod et al. 2024; Adams et al. 2024, grey circles).

lution<sup>6</sup>, we additionally provide a fit to these curves to estimate more accurately the end of reionization. We note that in the unconstrained case, all models reionize at different redshifts. Reionization is the fastest (at  $z = 6.4$ ) in the  $\sigma_8$  high model, as structure formation happens earlier. The  $\sigma_8$  low model is still only 45% reionized by  $z = 5$  because of the lack of sources, and shows the poorest agreement with observational constraints. In the constrained case, the differences are reduced, but still significant. In particular, we note that the  $\sigma_8$  low model reionizes the fastest at  $z = 5.75$ , while the  $\sigma_8$  high model is only  $\approx 65\%$  ionized by  $z = 5$ . This reversal of reionization histories with respect to the unconstrained case is due to the impact of different astrophysical parameters. Specifically, the significantly higher  $E_{\text{SN}}$

in the  $\sigma_8$  high model blows away gas and thus suppresses star formation, which consequently reduces the production of ionizing photons. On the other hand, the higher  $\alpha_{\text{SF}}$  and  $\alpha_{\text{SF,burst}}$  in the  $\sigma_8$  low model along with the lower  $E_{\text{SN}}$  significantly boosts star formation.

As the four models reionize at different redshifts and the end of the EoR can be observationally constrained (e.g., detections of Gunn-Peterson troughs in the Lyman- $\alpha$  forest as shown in Becker et al. 2015, Qin et al. 2021 and Bosman et al. 2022), this in turn limits the possible choice of astrophysical and cosmological parameters. We note that to model more realistically the final phases of reionization, the unresolved Lyman limit systems which govern absorption during the final stages of the reionization process should be accounted for (see Georgiev et al. 2024; Giri et al. 2024). These, though, are not included here.

Finally, the four models produce a Thomson scattering optical depth in the range (0.041-0.067) and (0.048-0.060) for the unconstrained and constrained case respectively, assuming an Helium (He) II fraction equal to the HII fraction, and an instantaneous HeII reionization at  $z = 3$ . These numbers are in agreement with *Planck* observations (Planck Collaboration et al. 2020; de Belsunce et al. 2021; Giarè et al. 2024).

### 3 RESULTS

In this section, we present the results from our simulations with respect to various galactic and IGM properties for the unconstrained and constrained case. To reduce the effect of cosmic variance, we always consider the A and B-series averages when comparing to observations.

#### 3.1 Unconstrained case

In the unconstrained case, we discuss the galactic and IGM observables for models with the UVLFs reported in the top panel of Figure 2.

##### 3.1.1 Galactic properties

In Figure 5, we present the mass-binned star formation rate (SFR) of galaxies in the four models at  $z = 10$  and  $9$ , with the top panel showing the unconstrained case. The solid lines are the median SFR, with the shaded regions referring to the 16th to 84th percentiles. The star formation main sequence (SFMS) in each case is additionally compared with results from various recent JWST programs represented by grey circles with a binning of  $\pm 0.25$  around the redshift. As all parameters affecting the star formation rate were kept the same across all four models, we note that the overall trends are similar, and agree with observations. The impact of matter clustering is seen at the low-mass end, where a larger clustering allows for the formation of a statistically significant sample of smaller mass galaxies in the  $\sigma_8$  high and  $h$  high models, while the smallest mass galaxies formed in the  $\sigma_8$  low case are an order of magnitude more massive. Further, at the high mass end, we note that the  $\sigma_8$  high model produces the most massive galaxies, which also have the highest SFR.

To confirm the agreement in star formation rates, in Figure 6 we additionally look at the global star formation efficiency (SFE) at the same redshifts with the top panel showing the unconstrained case. We define SFE as the ratio of the stellar and halo mass scaled by  $f_b = \Omega_b/\Omega_m$ , i.e.  $M_{\text{star}}/M_{\text{halo}}f_b$ , as a function of the halo mass  $M_{\text{halo}}$ . We also compare this to Spitzer observations at  $z = 7$  (Stefanon et al. 2021) and to abundance matching estimates from Tacchella

<sup>6</sup> While we have a large number of snapshots as discussed in Section 2.1 for the sake of simplicity, to run POLAR we adopt a uniform step size of  $\Delta z = 0.5$ .

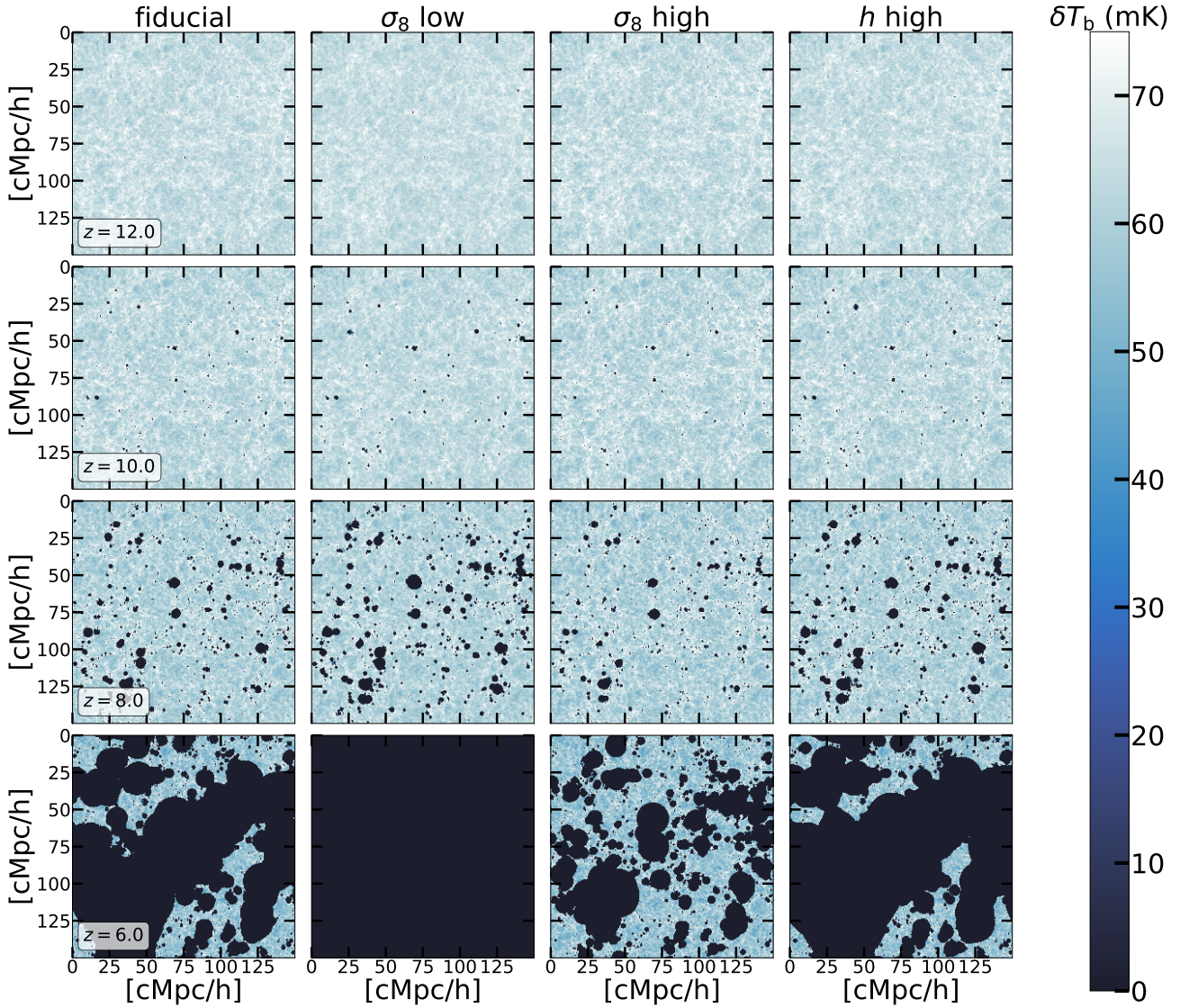


**Figure 3.** Maps of  $\delta T_b$  of the A-series middle slices of single cell thickness (i.e.,  $\approx 600 h^{-1}$  ckpc) for the four cosmological models in the constrained case at  $z = 12, 10, 8,$  and  $6$  (from top to bottom). Here the dark areas represent the ionized regions with  $\delta T_b = 0$ . Note that  $\delta T_b$  cannot have negative values due to the assumption of  $T_S \gg T_{CMB}$ .

et al. (2018). As mentioned above, the parameters controlling the star formation efficiency are the same across all models, and thus the corresponding global SFE is the same as well. The only difference is in the largest galaxies formed, which is directly proportional to  $\sigma_8$  as it controls the clustering of mass. We note that the SFE is marginally higher than the abundance matching estimates for the lower mass halos, but the difference is  $\lesssim 0.3$  dex. Further, the weak mass dependence of the global SFE trend is in agreement with zoom-in hydrodynamical simulations like FIREbox<sup>HR</sup> (Feldmann et al. 2024).

### 3.1.2 21-cm signal from the IGM

We note that despite the disagreement in UVLFs for the four cosmological models shown in the top panel of Figure 2, the models still reproduce fairly well observable quantities such as the SFR and global SFE, as shown in Section 3.1.1. Further, they are broadly in agreement with available data. We now look at IGM observables,

and more specifically at the 21-cm signal power spectrum (calculated according to Equation 4), shown in the top panel of Figure 7 for the unconstrained case at  $z = 9$ . At this redshift, we note from the top panel of Figure 4 that the reionization history is primarily governed by the matter clustering. Thus, the  $\sigma_8$  low model having the highest  $\langle x_{\text{HI}} \rangle$  suggests a significant contrast between its large neutral and ionized regions, thus leading to a higher power amplitude up to  $k = 0.40 h\text{Mpc}^{-1}$  as compared to the other three models. On the other hand, the greater matter clustering in the  $\sigma_8$  high and  $h$  high models leads to lower contrast at these scales due to more numerous ionized regions, and thus less power. However, at smaller scales, having more ionized regions allows for greater contrast, and thus the  $h$  high model catches up with the fiducial model, and the  $\sigma_8$  high model has the highest power overall at  $k > 0.40 h\text{Mpc}^{-1}$ .

For a better understanding of the 21-cm signal power spectrum evolution, in Figure 8 we additionally present its redshift dependence at large scales, i.e.  $k = 0.15 h\text{Mpc}^{-1}$ , with the top panel showing the unconstrained case. This allows us to compare how the 21-cm signal

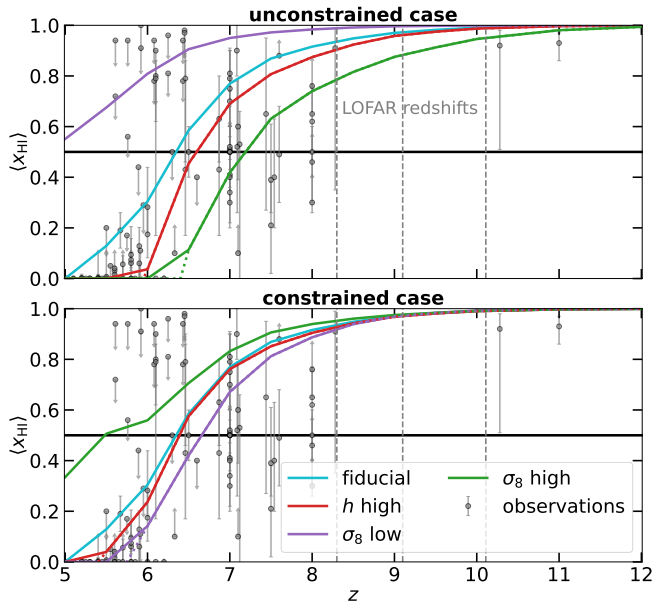


**Figure 4.** Redshift evolution of the average of the A and B-series volume-averaged neutral hydrogen fraction  $\langle x_{\text{HI}} \rangle$  for the fiducial (cyan),  $h$  high (red),  $\sigma_8$  low (purple) and  $\sigma_8$  high (green) models for the unconstrained (top) and constrained (bottom) cases. Dotted lines refer to a fit to the curves, which is used for a better estimate of the redshift of reionization when the redshift resolution is too coarse. The vertical grey dashed lines indicate the redshifts observationally relevant for LOFAR ( $z = 10.11, 9.16$  and  $8.3$ ), and the black solid line is drawn at  $\langle x_{\text{HI}} \rangle = 0.5$  to guide the eye. Grey circles are a collection of observational constraints (Fan et al. 2006; Totani et al. 2006; Ota et al. 2008; Ouchi et al. 2010; Bolton et al. 2011; Dijkstra et al. 2011; McGreer et al. 2011; Mortlock et al. 2011; Ono et al. 2012; Chornock et al. 2013; Jensen et al. 2013; Robertson et al. 2013; Schroeder et al. 2013; Pentericci et al. 2014; Schenker et al. 2014; McGreer et al. 2015; Sobacchi & Mesinger 2015; Choudhury et al. 2015; Mesinger et al. 2015; Greig et al. 2017; Davies et al. 2018; Mason et al. 2018; Hoag et al. 2019; Greig et al. 2019; Jones et al. 2024, collected in the CoRECON module, Garaldi 2023).

evolves in the four cosmological models across redshifts relevant to LOFAR observations. As suggested by the reionization histories, we note that the  $\sigma_8$  low model has a larger contrast due to slower reionization, and thus has a higher amplitude of  $\Delta_{21\text{cm}}^2$  ( $k = 0.15 \text{ h cMpc}^{-1}$ ) at the beginning of reionization. However, the  $\sigma_8$  high and  $h$  high models reach a higher amplitude by  $z \approx 8$  due to the formation of larger ionized regions.

### 3.2 Constrained case

As in this case we have also changed parameters that control star formation efficiency and supernova feedback, it is crucial to understand their impact on observables other than the UVLFs shown in the bottom panel of Figure 2.

#### 3.2.1 Galactic properties

As in Section 3.1.1, in the bottom panel of Figure 5 we look at the A and B-series averaged SFMS and compare them with observations from JWST at  $z = 10$  and 9 for the constrained case. We note that despite differences in the energy of supernovae ( $\alpha_{\text{SF}}$  and  $\alpha_{\text{SF,burst}}$  also differ for the  $\sigma_8$  low model), the high mass ends of the SFMS of the four models still agree with each other and with observations. This is because the most massive galaxies are also the most luminous,

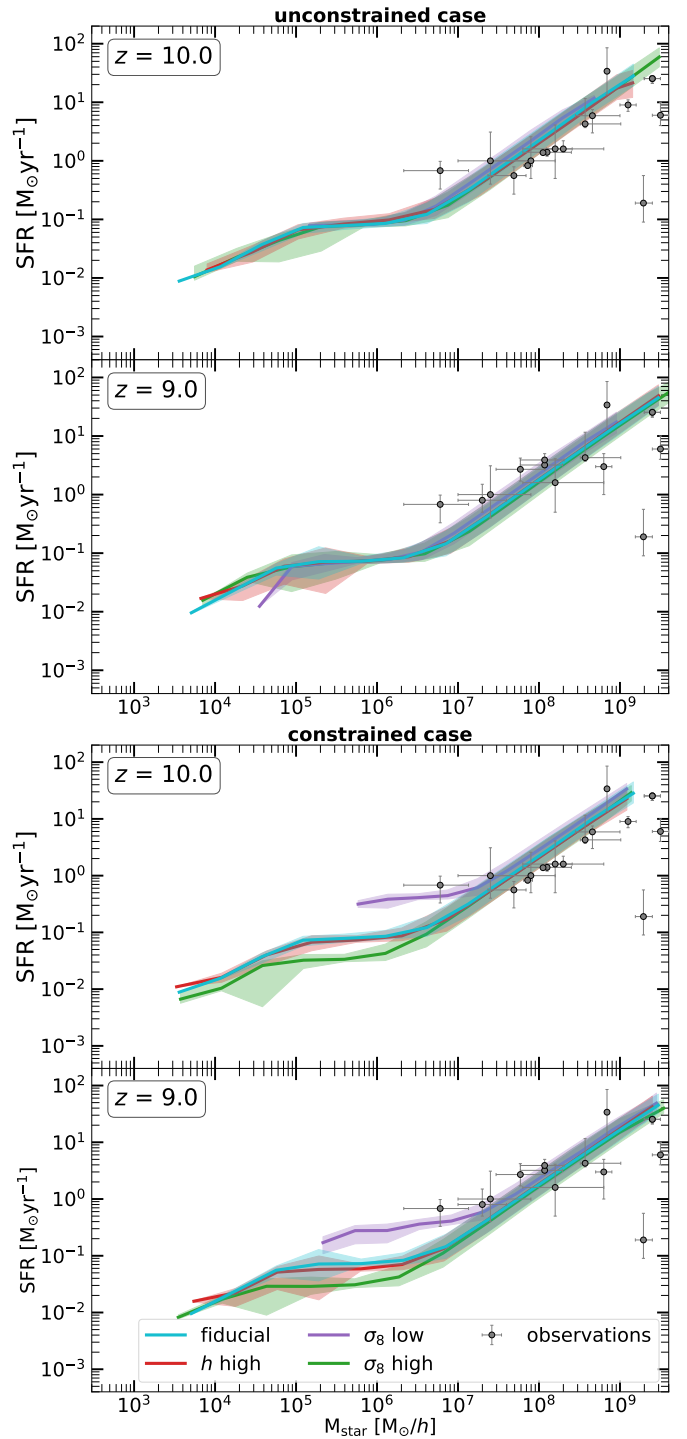


**Figure 5.** A and B-series averaged star formation rate (SFR) as a function of stellar mass for the unconstrained (top) and constrained (bottom) cases, for the fiducial (cyan),  $h$  high (red),  $\sigma_8$  low (purple) and  $\sigma_8$  high (green) models at  $z = 10$  and 9. Solid lines refer to the median star formation rate in each mass bin, with 16th and 84th percentiles shown as shaded regions. Grey circles are observations from various JWST programs (Treu et al. 2023; Fujimoto et al. 2023; Looser et al. 2023; Bouwens et al. 2023b; Papovich et al. 2023; Arrabal Haro et al. 2023b,a; Long et al. 2023; Leethochawalit et al. 2023; Atek et al. 2023; Robertson et al. 2023; Heintz et al. 2023a,b; Jin et al. 2023; Helton et al. 2024; Jung et al. 2024).



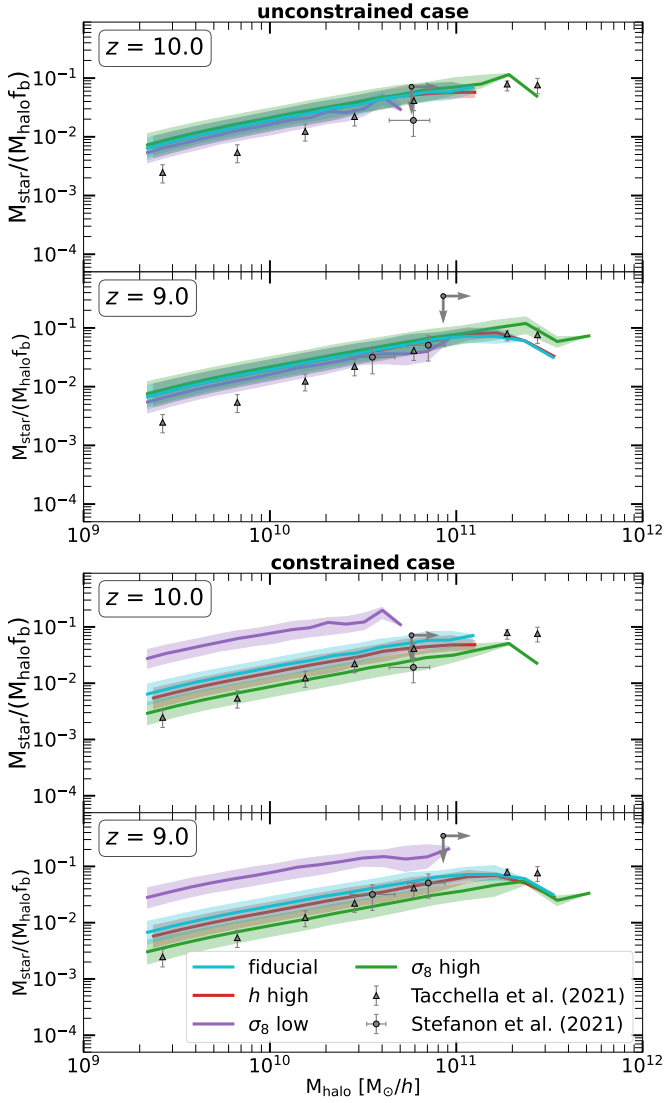


**Figure 6.** A and B-series averaged star formation efficiency (SFE) as a function of halo mass for the unconstrained (top) and constrained (bottom) cases, for the fiducial (cyan),  $h$  high (red),  $\sigma_8$  low (purple) and  $\sigma_8$  high (green) models at  $z = 10$  and  $9$ . Solid lines refer to the median SFE in each mass bin, with 16<sup>th</sup> and 84<sup>th</sup> percentiles shown as shaded regions. Grey circles are Spitzer observations from [Stefanon et al. \(2021\)](#), and grey triangles are abundance matching estimates from [Tacchella et al. \(2018\)](#).

and matching their UVLFs in Section 2.3 consequently matches their star formation properties. However, at the low-mass end, the SFMS of the four models shows some deviation at both redshifts. This is because at lower masses, the impact of astrophysical parameters starts to dominate, and while the  $\sigma_8$  high model forms galaxies with masses smaller than the  $\sigma_8$  low model, the median SFR of these low mass galaxies is an order of magnitude smaller than the lowest mass galaxies in the  $\sigma_8$  low model, because the impact of the energy released per supernova is sufficient to clear out gas and suppress star formation in the low-mass galaxies.

To further explore the impact of the energy released by supernovae, in the bottom panel of Figure 6 we also look at the global SFE for the constrained case. Here, we notice that, despite similar SFRs at the high-mass end, the efficiency of star formation in each case differs. The SFE for the  $\sigma_8$  low model is significantly boosted compared

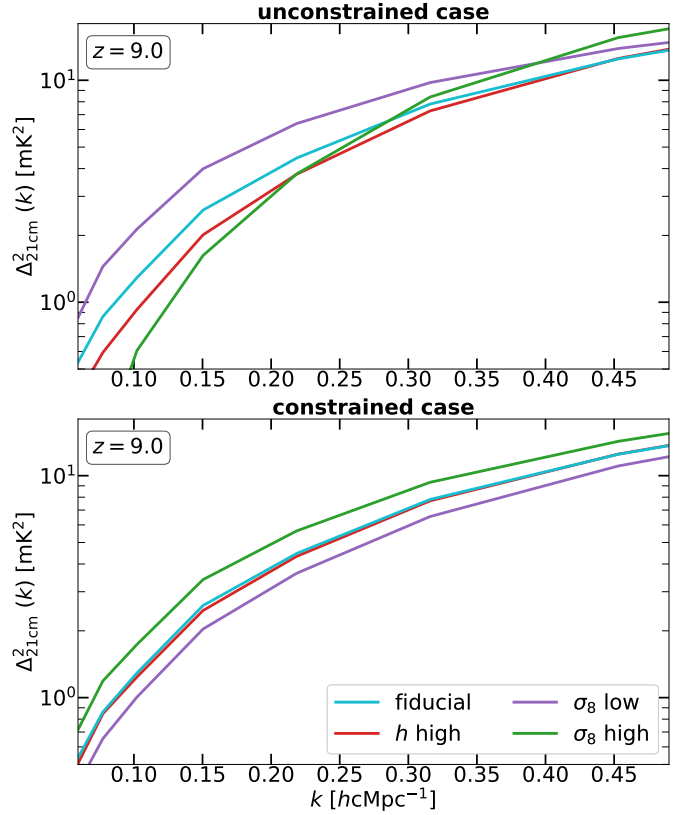


**Figure 7.** A and B-series averaged normalized 21-cm signal power spectrum ( $\Delta_{21\text{cm}}^2$ ) for the unconstrained (top) and constrained (bottom) cases, for the fiducial (cyan),  $h$  high (red),  $\sigma_8$  low (purple) and  $\sigma_8$  high (green) models at  $z = 9$ .

to observations, while the fiducial and  $h$  high models only mildly overpredict the observed SFE. The  $\sigma_8$  high case, on the other hand, is the best match. We note that the global SFE is inversely proportional to  $E_{\text{SN}}$  for all halo masses. The weak mass dependence trend of the SFE is the same of the unconstrained case, and in agreement with the trends of the FIREbox<sup>HR</sup> simulations ([Feldmann et al. 2024](#)) for the fiducial,  $\sigma_8$  high and  $h$  high models, while the  $\sigma_8$  low model is an order of magnitude higher but with the same slope.

### 3.2.2 21-cm signal from the IGM

While the UVLFs at  $M_{1600,AB} < -18$  in the constrained case are similar for all four cosmological models, the SFR and global SFE show differences, and in some cases do not match observations. In such a scenario, it becomes interesting to analyze the impact on the 21-cm signal, which is presented in the bottom panel of Figure 7 at  $z = 9$  for the constrained case. Unlike the unconstrained case where the differences in matter clustering contributed to differences not only in the overdensity term but also in the neutral hydrogen fraction term in equation 2, here the changes in astrophysical parameters lead to a drastic reduction in the differences between the value of  $\langle x_{\text{HI}} \rangle$  across the four models. Thus, the differences in the 21-cm signal power spectra of the four models are governed primarily by the overdensity term. This leads to a higher power across all wave modes for the  $\sigma_8$  high model due to greater matter clustering. While one would expect the  $h$  high model to have slightly higher power than the fiducial one due to the dependence on overdensity, the neutral-fraction term in Equation 2 reduces the contrast due to a marginally faster reionization

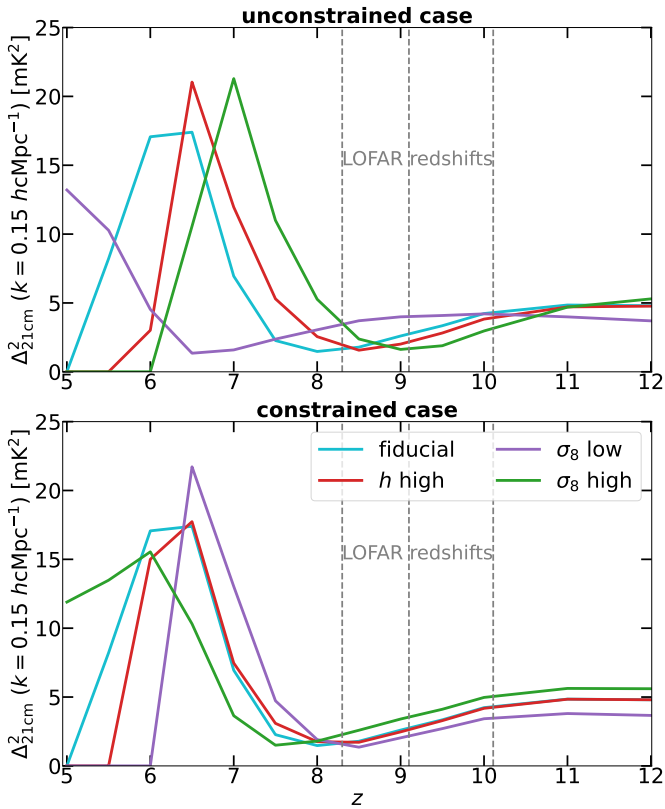


**Figure 8.** Redshift evolution of the A and B-series averaged normalized 21-cm signal power spectrum ( $\Delta_{21\text{cm}}^2$ ) at  $k = 0.15 \text{ hcMpc}^{-1}$  for the unconstrained (top) and constrained (bottom) cases, for the fiducial (cyan),  $h$  high (red),  $\sigma_8$  low (purple) and  $\sigma_8$  high (green) models. The vertical dashed lines indicate the redshifts relevant for LOFAR, i.e.  $z = 10.11, 9.16,$  and  $8.3$ .

process, so that the power in the two cases becomes similar. Even the  $\sigma_8$  low model matches the fiducial and  $h$  high models’ power spectra due to a faster reionization process.

In the bottom panel of Figure 8, we present the redshift evolution of the 21-cm signal power spectrum at  $k = 0.15 \text{ hcMpc}^{-1}$  for the constrained case and notice a significant reduction in the differences of  $\Delta_{21\text{cm}}^2$  ( $k = 0.15 \text{ hcMpc}^{-1}$ ) values between the various cosmological models at  $12 > z > 5$  compared to the extent of differences in the unconstrained case (top panel of Figure 8). Indeed, at  $10 > z > 8.5$ , where LOFAR observations are focused, variations in the  $\sigma_8$  parameter lead to differences in the power spectrum of only a few  $\text{mK}^2$ . While the exact magnitude of the difference is subject to the position of the peak of  $\Delta_{21\text{cm}}^2$  ( $k = 0.15 \text{ hcMpc}^{-1}$ ), which in turn is governed by modeling assumptions like the choice of  $f_{\text{esc}}$  (see Appendix C for a comparison between  $f_{\text{esc}} = 12.5\%$  and  $25\%$ ), the key takeaway is that *significantly different choices of cosmological and astrophysical parameters can still lead to similar 21-cm signal observables, even when constrained by the UVLFs from JWST and HST observations.* Thus, to explore the parameter space of models that agree with upper limits of 21-cm signal power spectra observations at the redshifts of interest to LOFAR, one should still consider various cosmological and astrophysical parameters as free. However, jointly constraining these models with a more diverse set of galactic observables from JWST and upcoming surveys with Euclid and SPHEREx can allow us to narrow down the choice of viable ones. Additionally, tomographic imaging of the distribution of neutral Hydrogen with the upcoming SKA-Low could also be used for additional constraints on

IGM properties from images such as those shown in Figure 3 (see for e.g. Bianco et al. 2021).

## 4 DISCUSSION

By analyzing various galactic and IGM observables, we note that the interplay of astrophysical and cosmological parameters can lead to similarities as well as differences. For example, in the constrained case, while agreement with observed UVLFs leads to similar SFR for the high-mass galaxies across all models, there are significant differences in the SFR and global SFE for low-mass galaxies. On the other hand, while in the unconstrained case the SFR and global SFE show a very similar dependence on stellar mass in all models because the parameters that regulate such quantities are the same, the UVLFs exhibit significant differences.

For the IGM, we note that the 21-cm signal power spectrum at the redshifts of interest for LOFAR is very similar across all four models in the constrained case (bottom panel, Figure 7). This is due to the choice of astrophysical parameters, which reduces the impact of the cosmological ones, and consequently the differences between the reionization histories in comparison to the unconstrained case. In the unconstrained case, we note significant differences in reionization histories simply because the choice of cosmological parameters changes the overall matter clustering.

These similarities in terms of 21-cm observables have a profound impact on inference modeling, as models with very different cosmological and astrophysical parameters may still produce 21-cm signal power spectra in agreement with current upper limits (for example from Mertens et al. 2020; Trott et al. 2020; HERA Collaboration et al. 2023; Acharya et al. 2024c), or possibly also with an eventual measurement. This is because, while the end of reionization may differ among models, at  $z > 7$  the extent and speed of reionization are still largely similar. This means that fixing a priori any of these parameters could exclude viable models. While introducing cosmological and astrophysical parameters as free parameters during inference modeling has been attempted in several earlier studies (see e.g. Kern et al. 2017; Schneider et al. 2023), these have used only approximate reionization simulation codes due to the significant computational costs involved in building such a high-dimensional parameter space. Indeed, in a more physical approach, it is necessary to run a large number of dark-matter only simulations with different cosmologies, each post-processed with a large set of astrophysical parameters. The problem worsens if one would like to boost the resolution of the simulations to take into account the role of mini halos (see Haiman et al. 2001; Iliiev et al. 2005), dwarf galaxies (Wu & Kravtsov 2024), or Lyman Limit Systems (Georgiev et al. 2024; Giri et al. 2024) which likely play a significant role in the EoR. While faster semi-numerical codes and emulators can be employed, they are not ideal tools to model galaxy-scale physics and radiative transfer effects.

Because of this, boosting the resolution of low-resolution simulations using analytic techniques based on smaller boxes with higher resolution has been proposed (see for example Nasirudin et al. 2020; Barsode & Choudhury 2024). Newer methods based on Machine Learning, such as Generative Adversarial Networks (GANs, as done in Zhang et al. 2024), bypass the requirement of a higher resolution simulation. However, it needs to be explored whether such methods are robust enough to factor in small differences in individual parameters. In subsequent work with POLAR, we intend to include resolution-boosting techniques to resolve halos and galaxies down by at least two orders of magnitude in mass. The development and implementation of such techniques will additionally allow us to create more

diverse training sets of power spectra for building Machine Learning kernels for Gaussian Process Regression based signal extraction, as shown by Mertens et al. (2024) and Acharya et al. (2024a,c).

## 5 SUMMARY

In this work, we have investigated the impact of different cosmological models on the 21-cm signal and some galactic properties using POLAR, which combines  $N$ -body dark matter simulations run with GADGET-4 with the semi-analytic model of galaxy formation L-GALAXIES, and the 1-D radiative transfer code GRIZZLY. We have applied the framework to four different cosmological models: a “fiducial” model, which adopts values of the cosmological parameters from Planck Collaboration et al. (2020); a “ $h$  high” model, with  $h = 0.733$  based on results from studies of Cepheid variables in the host galaxies of 42 Type Ia supernovae (Riess et al. 2022); a “ $\sigma_8$  low” case, with  $\sigma_8 = 0.702$  from an anisotropic galaxy clustering measurement analysis done by Tröster et al. (2020); and a “ $\sigma_8$  high” case, with  $\sigma_8 = 0.880$  according to recent eROSITA results (Ghirardini et al. 2024). We additionally used the Fixed & Paired approach (Angulo & Pontzen 2016) to suppress cosmic variance by boosting the effective volumes of the simulations. For all the quantities analyzed, we took an average of the fixed initial conditions case (which we refer to as the A-series) and its corresponding pair (referred to as the B-series).

We then choose astrophysical parameters in L-GALAXIES such that the fiducial model matches UV luminosity functions from HST legacy fields and JWST programs at  $z = 10$  and  $9$ . To investigate the effect of adopting different values for  $h$  and  $\sigma_8$  on other galactic and IGM observables, we use the same astrophysical parameters also for the other three cosmological models. We refer to this as the “unconstrained” case, as by not changing astrophysical parameters for the different cosmological models the resulting UVLFs will not necessarily be consistent with the observed ones. We also built a “constrained” case, where we instead choose the astrophysical parameters such that the UVLFs obtained in each cosmological model are consistent with those observed at  $z = 10$  and  $9$ . For this, we increased the star formation efficiency and reduced the energy released per supernova in the  $\sigma_8$  low model to boost star formation and, in turn, its UVLF. On the other hand, we increased the energy released per supernova for the  $h$  high and  $\sigma_8$  high models to suppress star formation and mitigate the impact of increased matter clustering as compared to the fiducial model. For the radiative transfer calculations, we only took into account the stellar sources while modeling the spectral energy distributions and chose a global escape fraction of 12.5% across all redshifts for all four models.

Our results can be summarized as follows:

- **Reionization history:** In the unconstrained case, the values of the cosmological parameters strongly influence the matter clustering, which in turn leads to significant differences in how reionization progresses in each model. While the  $\sigma_8$  high model reionizes by  $z \approx 6.4$ , the  $\sigma_8$  low model is only 45% reionized even by  $z = 5$ . In the constrained case, instead, the impact of astrophysical parameters is significant, and the  $\sigma_8$  low model is the first to reionize, at  $z = 5.75$ , while the  $\sigma_8$  high model is only 70% reionized by  $z = 5$ .

- **Star Formation Rate (SFR):** In the unconstrained case, no significant differences are observed as the parameters controlling star formation have been kept the same. However, in the constrained case the SFR in low-mass galaxies is impacted by the required energy released per supernova, and thus the SFR is boosted for the  $\sigma_8$  low

model and suppressed for the  $\sigma_8$  high model. In both cases, all models broadly agree with observations at  $z = 10$  and  $9$ .

- **Global Star Formation Efficiency (SFE):** As the parameters controlling star formation are the same in the unconstrained case, the global SFE at all masses is similar in all models. The SFE is also in agreement with observations and abundance matching estimates. However, in the constrained case, due to a higher value of the parameter regulating the star formation efficiency, the global SFE in the  $\sigma_8$  low model is also higher. The other three models show minor differences, governed by the differences in the energy released per supernova.

- **21-cm signal power spectrum:** In the unconstrained case, the differences between the four models are not only due to the difference in overdensity but also to those in the neutral fraction and its redshift evolution. However, in the constrained case, the neutral fraction at  $z > 8$  is similar in all models, as the impact of matter clustering on the neutral fraction is canceled out by the impact of setting different values for the astrophysical parameters controlling star formation. Thus, the power spectrum at higher redshifts is mostly dictated by the overdensity term, and because of this it shows smaller differences among the four models.

Overall, we conclude that different values of cosmological and astrophysical parameters can lead to differences in some observables (e.g. low-mass SFR and global SFE), while others are largely unaffected (e.g. UVLFs and 21-cm signal power spectrum). In particular, we note that despite significantly different galactic processes and reionization histories, the 21-cm power spectra are very similar in power across  $k$ -bins and in agreement with current observational upper limits (Acharya et al. 2024c; Mertens et al. 2020; Trott et al. 2020; HERA Collaboration et al. 2023). Due to this, when doing inference modeling, it is essential to consider all cosmological and astrophysical parameters as free parameters, with other observational constraints serving as priors. While a limited exploration of astrophysical parameters can be done with excursion set algorithms, a semi-analytic model provides a significantly more rigorous and physical approach to modeling galactic properties. For varying cosmological parameters though, it is necessary to run a large number of  $N$ -body simulations to populate the prior parameter space. However, running so many high-resolution simulations would be prohibitively expensive in terms of computational resources and time. To address this issue, in future work we intend to incorporate techniques for boosting the resolution of less costly, low-resolution simulations using either analytic or machine learning techniques. Such an implementation would also additionally allow us to build broader training sets of power spectra for the Machine Learning kernels used with Gaussian Process Regression by the LOFAR EoR Key Science Project team (as done by Acharya et al. 2024a).

Lastly, to achieve a stronger constraining power on a broadened parameter space, it is essential to jointly employ a variety of galactic observables, e.g. from JWST, Euclid and upcoming SPHEREx, as well as tomographic imaging of neutral Hydrogen in the IGM with the future SKA-Low.

## ACKNOWLEDGEMENTS

AA thanks the EoR research group at MPA, Volker Springel and Rüdiger Pakmor for helpful discussions. AA acknowledges Nordita’s PhD Fellows Visitor program for funding a part of this work, and thanks Nordita for their hospitality. Nordita is supported in part by NordForsk. RG acknowledges support from SERB, DST Ramanujan Fellowship no. RJF/2022/000141. GM is supported by the Swedish

Research Council project grant 2020-04691\_VR. SZ acknowledges the Alexander von Humboldt Foundation for the Humboldt Research Award and the Max Planck Institute for Astrophysics for its hospitality. The post-doctoral contract of IH was funded by Sorbonne Université in the framework of the Initiative Physique des Infinis (IDEX SUPER). LVEK acknowledges the financial support from the European Research Council (ERC) under the European Union’s Horizon 2020 research and innovation programme (Grant agreement No. 884760, ‘CoDEX’).

This work used the color map “arctic” for slice images from the publicly available Python package CMASHER (van der Velden 2020) and the Python package CoReCon (Garaldi 2023) for collating neutral fraction observations. Additionally, this work made extensive use of commonly used packages like NUMPY (Harris et al. 2020), MATPLOTLIB (Hunter 2007) and SCIPY (Virtanen et al. 2020).

## DATA AVAILABILITY

The simulation data, and post-analysis scripts used in this work can be shared upon reasonable request to the corresponding author.

## REFERENCES

- Abdurashidova Z., et al., 2022, *ApJ*, 924, 51  
 Acharya A., et al., 2024a, *MNRAS*, 527, 7835  
 Acharya A., Garaldi E., Ciardi B., Ma Q.-b., 2024b, *MNRAS*, 529, 3793  
 Acharya A., Mertens F., Ciardi B., Ghara R., Koopmans L. V. E., Zaroubi S., 2024c, *MNRAS*, 534, L30  
 Adams N. J., et al., 2024, *ApJ*, 965, 169  
 Anderson L., Pontzen A., Font-Ribera A., Villaescusa-Navarro F., Rogers K. K., Genel S., 2019, *ApJ*, 871, 144  
 Angulo R. E., Pontzen A., 2016, *MNRAS*, 462, L1  
 Arrabal Haro P., et al., 2023a, *Nature*, 622, 707  
 Arrabal Haro P., et al., 2023b, *ApJ*, 951, L22  
 Atek H., et al., 2023, *MNRAS*, 524, 5486  
 Balu S., Greig B., Qiu Y., Power C., Qin Y., Mutch S., Wyithe J. S. B., 2023, *MNRAS*, 520, 3368  
 Barrera M., et al., 2023, *MNRAS*, 525, 6312  
 Barsode A., Choudhury T. R., 2024, arXiv e-prints, p. arXiv:2407.10585  
 Basu A., Garaldi E., Ciardi B., 2024, *MNRAS*, 532, 841  
 Becker G. D., Bolton J. S., Madau P., Pettini M., Ryan-Weber E. V., Venemans B. P., 2015, *MNRAS*, 447, 3402  
 Bhagwat A., Costa T., Ciardi B., Pakmor R., Garaldi E., 2024, *MNRAS*, 531, 3406  
 Bianco M., Giri S. K., Iliev I. T., Mellema G., 2021, *MNRAS*, 505, 3982  
 Bird S., Ni Y., Di Matteo T., Croft R., Feng Y., Chen N., 2022, *MNRAS*, 512, 3703  
 Bolton J. S., Haehnelt M. G., Warren S. J., Hewett P. C., Mortlock D. J., Venemans B. P., McMahon R. G., Simpson C., 2011, *MNRAS*, 416, L70  
 Bosman S. E. I., et al., 2022, *MNRAS*, 514, 55  
 Bouwens R. J., et al., 2015, *ApJ*, 803, 34  
 Bouwens R. J., et al., 2021, *AJ*, 162, 47  
 Bouwens R., Illingworth G., Oesch P., Stefanon M., Naidu R., van Leeuwen I., Magee D., 2023a, *MNRAS*, 523, 1009  
 Bouwens R. J., et al., 2023b, *MNRAS*, 523, 1036  
 Carniani S., et al., 2024, arXiv e-prints, p. arXiv:2405.18485  
 Casavecchia B., Maio U., Péroux C., Ciardi B., 2024, *A&A*, 689, A106  
 Chartier N., Wandelt B., Akrami Y., Villaescusa-Navarro F., 2021, *MNRAS*, 503, 1897  
 Chornock R., Berger E., Fox D. B., Lunnan R., Drout M. R., Fong W.-f., Laskar T., Roth K. C., 2013, *ApJ*, 774, 26  
 Choudhury T. R., Puchwein E., Haehnelt M. G., Bolton J. S., 2015, *MNRAS*, 452, 261  
 Choudhury M., et al., 2024, arXiv e-prints, p. arXiv:2407.03523  
 Ciardi B., Madau P., 2003, *ApJ*, 596, 1  
 Davies F. B., et al., 2018, *ApJ*, 864, 142  
 Dijkstra M., Mesinger A., Wyithe J. S. B., 2011, *MNRAS*, 414, 2139  
 Dixon K. L., Iliev I. T., Mellema G., Ahn K., Shapiro P. R., 2016, *MNRAS*, 456, 3011  
 Eide M. B., Graziani L., Ciardi B., Feng Y., Kakiichi K., Di Matteo T., 2018, *MNRAS*, 476, 1174  
 Eide M. B., Ciardi B., Graziani L., Busch P., Feng Y., Di Matteo T., 2020, *MNRAS*, 498, 6083  
 Esmerian C. J., Gnedin N. Y., 2021, *ApJ*, 910, 117  
 Esmerian C. J., Gnedin N. Y., 2022, *ApJ*, 940, 74  
 Esmerian C. J., Gnedin N. Y., 2024, *ApJ*, 968, 113  
 Fan X., et al., 2006, *AJ*, 132, 117  
 Feldmann R., et al., 2024, arXiv e-prints, p. arXiv:2407.02674  
 Field G. B., 1959, *ApJ*, 129, 551  
 Finkelstein S. L., et al., 2015, *ApJ*, 810, 71  
 Finlator K., Keating L., Oppenheimer B. D., Davé R., Zackrisson E., 2018, *MNRAS*, 480, 2628  
 Fujimoto S., et al., 2023, *ApJ*, 949, L25  
 Furlanetto S. R., Oh S. P., Pierpaoli E., 2006, *Phys. Rev. D*, 74, 103502  
 Garaldi E., 2023, *The Journal of Open Source Software*, 8, 5407  
 Garaldi E., Kannan R., Smith A., Springel V., Pakmor R., Vogelsberger M., Hernquist L., 2022, *MNRAS*, 512, 4909  
 Garaldi E., et al., 2024, *MNRAS*, 530, 3765  
 Georgiev I., Mellema G., Giri S. K., 2024, arXiv e-prints, p. arXiv:2405.04273  
 Ghara R., Choudhury T. R., Datta K. K., 2015, *MNRAS*, 447, 1806  
 Ghara R., Mellema G., Giri S. K., Choudhury T. R., Datta K. K., Majumdar S., 2018, *MNRAS*, 476, 1741  
 Ghara R., et al., 2020, *MNRAS*, 493, 4728  
 Ghara R., et al., 2024, *A&A*, 687, A252  
 Ghirardini V., et al., 2024, arXiv e-prints, p. arXiv:2402.08458  
 Giare W., Di Valentino E., Melchiorri A., 2024, *Phys. Rev. D*, 109, 103519  
 Giri S. K., Mellema G., 2021, *MNRAS*, 505, 1863  
 Giri S. K., Mellema G., Aldheimer T., Dixon K. L., Iliev I. T., 2019a, *MNRAS*, 489, 1590  
 Giri S. K., D’Aloisio A., Mellema G., Komatsu E., Ghara R., Majumdar S., 2019b, *J. Cosmology Astropart. Phys.*, 2019, 058  
 Giri S. K., Schneider A., Maion F., Angulo R. E., 2023, *A&A*, 669, A6  
 Giri S. K., Bianco M., Schaeffer T., Iliev I. T., Mellema G., Schneider A., 2024, *MNRAS*, 533, 2364  
 Gnedin N. Y., 2014, *ApJ*, 793, 29  
 Gnedin N. Y., Kaurov A. A., 2014, *ApJ*, 793, 30  
 Greig B., Mesinger A., Haiman Z., Simcoe R. A., 2017, *MNRAS*, 466, 4239  
 Greig B., Mesinger A., Bañados E., 2019, *MNRAS*, 484, 5094  
 Greig B., Trott C. M., Barry N., Mutch S. J., Pindor B., Webster R. L., Wyithe J. S. B., 2021a, *MNRAS*, 500, 5322  
 Greig B., et al., 2021b, *MNRAS*, 501, 1  
 Greig B., Prelogović D., Qin Y., Ting Y.-S., Mesinger A., 2024, *MNRAS*, 533, 2530  
 HERA Collaboration et al., 2023, *ApJ*, 945, 124  
 Haiman Z., Abel T., Madau P., 2001, *ApJ*, 551, 599  
 Han J., Cole S., Frenk C. S., Benitez-Llambay A., Helly J., 2018, *MNRAS*, 474, 604  
 Harikane Y., et al., 2022, *ApJS*, 259, 20  
 Harikane Y., et al., 2023, *ApJS*, 265, 5  
 Harris C. R., et al., 2020, *Nature*, 585, 357  
 Heintz K. E., et al., 2023a, arXiv e-prints, p. arXiv:2306.00647  
 Heintz K. E., et al., 2023b, *Nature Astronomy*, 7, 1517  
 Helton J. M., et al., 2024, *ApJ*, 962, 124  
 Henriques B. M. B., White S. D. M., Thomas P. A., Angulo R., Guo Q., Lemson G., Springel V., Overzier R., 2015, *MNRAS*, 451, 2663  
 Henriques B. M. B., Yates R. M., Fu J., Guo Q., Kauffmann G., Srisawat C., Thomas P. A., White S. D. M., 2020, *MNRAS*, 491, 5795  
 Hernández-Aguayo C., et al., 2023, *MNRAS*, 524, 2556  
 Hirling P., Bianco M., Giri S. K., Iliev I. T., Mellema G., Kneib J. P., 2024, *Astronomy and Computing*, 48, 100861  
 Hoag A., et al., 2019, *ApJ*, 878, 12  
 Hogan C. J., Rees M. J., 1979, *MNRAS*, 188, 791

- Hothi I., Allys E., Semelin B., Boulanger F., 2024, *A&A*, **686**, A212
- Hunter J. D., 2007, *Computing in Science & Engineering*, **9**, 90
- Hutter A., Dayal P., Yepes G., Gottlöber S., Legrand L., Ucci G., 2021, *MNRAS*, **503**, 3698
- Hutter A., Cueto E. R., Dayal P., Gottlöber S., Trebitsch M., Yepes G., 2024, *arXiv e-prints*, p. [arXiv:2410.00730](https://arxiv.org/abs/2410.00730)
- Iliev I. T., Shapiro P. R., Raga A. C., 2005, *MNRAS*, **361**, 405
- Iliev I. T., Mellema G., Ahn K., Shapiro P. R., Mao Y., Pen U.-L., 2014, *MNRAS*, **439**, 725
- Jensen H., Laursen P., Mellema G., Iliev I. T., Sommer-Larsen J., Shapiro P. R., 2013, *MNRAS*, **428**, 1366
- Lin S., et al., 2023, *A&A*, **670**, L11
- Jones G. C., et al., 2024, *arXiv e-prints*, p. [arXiv:2409.06405](https://arxiv.org/abs/2409.06405)
- Jung I., et al., 2024, *ApJ*, **967**, 73
- Kannan R., Garaldi E., Smith A., Pakmor R., Springel V., Vogelsberger M., Hernquist L., 2022, *MNRAS*, **511**, 4005
- Kaur H. D., Gillet N., Mesinger A., 2020, *MNRAS*, **495**, 2354
- Kern N. S., Liu A., Parsons A. R., Mesinger A., Greig B., 2017, *ApJ*, **848**, 23
- Klypin A., Prada F., Byun J., 2020, *MNRAS*, **496**, 3862
- Koopmans L., et al., 2015, in *Advancing Astrophysics with the Square Kilometre Array (AASKA14)*. p. 1 ([arXiv:1505.07568](https://arxiv.org/abs/1505.07568)), doi:10.22323/1.215.0001
- Kostyuk I., Nelson D., Ciardi B., Glatzle M., Pillepich A., 2023, *MNRAS*, **521**, 3077
- Leethochawalit N., et al., 2023, *ApJ*, **942**, L26
- Leung G. C. K., et al., 2023, *ApJ*, **954**, L46
- Lewis J. S. W., et al., 2022, *MNRAS*, **516**, 3389
- Long A. S., et al., 2023, *arXiv e-prints*, p. [arXiv:2305.04662](https://arxiv.org/abs/2305.04662)
- Looser T. J., et al., 2023, *arXiv e-prints*, p. [arXiv:2306.02470](https://arxiv.org/abs/2306.02470)
- Ma X., et al., 2018, *MNRAS*, **478**, 1694
- Ma Q.-B., Ciardi B., Eide M. B., Busch P., Mao Y., Zhi Q.-J., 2021, *ApJ*, **912**, 143
- Ma Q.-B., Ghara R., Ciardi B., Iliev I. T., Koopmans L. V. E., Mellema G., Mondal R., Zaroubi S., 2023, *MNRAS*, **522**, 3284
- Madau P., Meiksin A., Rees M. J., 1997, *ApJ*, **475**, 429
- Maio U., Péroux C., Ciardi B., 2022, *A&A*, **657**, A47
- Maion F., Angulo R. E., Zennaro M., 2022, *J. Cosmology Astropart. Phys.*, **2022**, 036
- Mason C. A., et al., 2018, *ApJ*, **857**, L11
- McGreer I. D., Mesinger A., Fan X., 2011, *MNRAS*, **415**, 3237
- McGreer I. D., Mesinger A., D'Odorico V., 2015, *MNRAS*, **447**, 499
- McLeod D. J., et al., 2024, *MNRAS*, **527**, 5004
- Mellema G., Iliev I. T., Alvarez M. A., Shapiro P. R., 2006, *New Astron.*, **11**, 374
- Mertens F. G., et al., 2020, *MNRAS*, **493**, 1662
- Mertens F. G., Bobin J., Carucci I. P., 2024, *MNRAS*, **527**, 3517
- Mesinger A., Furlanetto S., 2007, *ApJ*, **669**, 663
- Mesinger A., Furlanetto S., Cen R., 2011, *MNRAS*, **411**, 955
- Mesinger A., Aykutalp A., Vanzella E., Pentericci L., Ferrara A., Dijkstra M., 2015, *MNRAS*, **446**, 566
- Molaro M., Davé R., Hassan S., Santos M. G., Finlator K., 2019, *MNRAS*, **489**, 5594
- Mondal R., Bharadwaj S., Majumdar S., 2017, *MNRAS*, **464**, 2992
- Mondal R., et al., 2020, *MNRAS*, **498**, 4178
- Mortlock D. J., et al., 2011, *Nature*, **474**, 616
- Murray S., 2014, HMF: Halo Mass Function calculator, Astrophysics Source Code Library, record ascl:1412.006
- Mutch S. J., Geil P. M., Poole G. B., Angel P. W., Duffy A. R., Mesinger A., Wyithe J. S. B., 2016, *MNRAS*, **462**, 250
- Nasirudin A., Iliev I. T., Ahn K., 2020, *MNRAS*, **494**, 3294
- Ocvirk P., et al., 2016, *MNRAS*, **463**, 1462
- Ocvirk P., et al., 2020, *MNRAS*, **496**, 4087
- Ono Y., et al., 2012, *ApJ*, **744**, 83
- Ota K., et al., 2008, *ApJ*, **677**, 12
- Ouchi M., et al., 2010, *ApJ*, **723**, 869
- Papovich C., et al., 2023, *ApJ*, **949**, L18
- Peacock J. A., 1999, *Cosmological Physics*
- Pentericci L., et al., 2014, *ApJ*, **793**, 113
- Planck Collaboration et al., 2020, *A&A*, **641**, A6
- Qin Y., Mesinger A., Bosman S. E. I., Viel M., 2021, *MNRAS*, **506**, 2390
- Riess A. G., et al., 2022, *ApJ*, **934**, L7
- Robertson B. E., et al., 2013, *ApJ*, **768**, 71
- Robertson B. E., et al., 2023, *Nature Astronomy*, **7**, 611
- Rosdahl J., et al., 2018, *MNRAS*, **479**, 994
- Santos M., Ferramacho L., Silva M., Amblard A., Cooray A., 2010a, SimFast21: Simulation of the Cosmological 21cm Signal, Astrophysics Source Code Library, record ascl:1010.025
- Santos M. G., Ferramacho L., Silva M. B., Amblard A., Cooray A., 2010b, *MNRAS*, **406**, 2421
- Saxena A., Cole A., Gazagnes S., Meerburg P. D., Weniger C., Witte S. J., 2023, *MNRAS*, **525**, 6097
- Schaeffer T., Giri S. K., Schneider A., 2023, *MNRAS*, **526**, 2942
- Schenker M. A., Ellis R. S., Konidaris N. P., Stark D. P., 2014, *ApJ*, **795**, 20
- Schneider A., Schaeffer T., Giri S. K., 2023, *Phys. Rev. D*, **108**, 043030
- Schroeder J., Mesinger A., Haiman Z., 2013, *MNRAS*, **428**, 3058
- Shaver P. A., Windhorst R. A., Madau P., de Bruyn A. G., 1999, *A&A*, **345**, 380
- Smith A., Kannan R., Garaldi E., Vogelsberger M., Pakmor R., Springel V., Hernquist L., 2022, *MNRAS*, **512**, 3243
- Sobacchi E., Mesinger A., 2015, *MNRAS*, **453**, 1843
- Springel V., White S. D. M., Tormen G., Kauffmann G., 2001, *MNRAS*, **328**, 726
- Springel V., Pakmor R., Zier O., Reinecke M., 2021, *MNRAS*, **506**, 2871
- Stanway E. R., Eldridge J. J., 2018, *MNRAS*, **479**, 75
- Stefanon M., Bouwens R. J., Labbé I., Illingworth G. D., Gonzalez V., Oesch P. A., 2021, *ApJ*, **922**, 29
- Tacchella S., Bose S., Conroy C., Eisenstein D. J., Johnson B. D., 2018, *ApJ*, **868**, 92
- Thomas R. M., et al., 2009, *MNRAS*, **393**, 32
- Tinker J., Kravtsov A. V., Klypin A., Abazajian K., Warren M., Yepes G., Gottlöber S., Holz D. E., 2008, *ApJ*, **688**, 709
- Totani T., Kawai N., Kosugi G., Aoki K., Yamada T., Iye M., Ohta K., Hattori T., 2006, *PASJ*, **58**, 485
- Tozzi P., Madau P., Meiksin A., Rees M. J., 2000, *ApJ*, **528**, 597
- Trac H., Chen N., Holst I., Alvarez M. A., Cen R., 2022, *ApJ*, **927**, 186
- Treu T., et al., 2023, *ApJ*, **942**, L28
- Tröster T., et al., 2020, *A&A*, **633**, L10
- Trott C. M., et al., 2020, *MNRAS*, **493**, 4711
- Vani A., Ayromlou M., Kauffmann G., Springel V., 2024, *arXiv e-prints*, p. [arXiv:2408.00824](https://arxiv.org/abs/2408.00824)
- Villaescusa-Navarro F., et al., 2018, *ApJ*, **867**, 137
- Virtanen P., et al., 2020, *Nature Methods*, **17**, 261
- Watson W. A., Iliev I. T., D'Aloisio A., Knebe A., Shapiro P. R., Yepes G., 2013, *Monthly Notices of the Royal Astronomical Society*, **433**, 1230–1245
- Wu Z., Kravtsov A., 2024, *The Open Journal of Astrophysics*, **7**, 56
- Zaroubi S., 2013, *The Epoch of Reionization*. Springer Berlin Heidelberg, Berlin, Heidelberg, pp 45–101, doi:10.1007/978-3-642-32362-1\_2, [https://doi.org/10.1007/978-3-642-32362-1\\_2](https://doi.org/10.1007/978-3-642-32362-1_2)
- Zhang X., Lachance P., Ni Y., Li Y., Croft R. A. C., Matteo T. D., Bird S., Feng Y., 2024, *MNRAS*, **528**, 281
- de Belsunce R., Gratton S., Coulton W., Efstathiou G., 2021, *MNRAS*, **507**, 1072
- van der Velden E., 2020, *The Journal of Open Source Software*, **5**, 2004

## APPENDIX A: UV LUMINOSITY FUNCTIONS ACROSS REDSHIFTS

As we tune the astrophysical parameters for the constrained case only to match the UVLFs at  $z = 10$  and  $9$ , it is interesting to explore how the four cosmological models compare to the UVLFs observed at other redshifts. In Figure A1, we show results at  $z = 12, 10, 9, 8, 7, 5$ . We note that while the models mildly overestimate observational data at  $z = 5$ , this could be because astrophysical parameters may need to be evolved with redshift, while here they are kept constant. Interestingly, the  $\sigma_8$  low model tends to reproduce the bright end much better at lower redshifts.

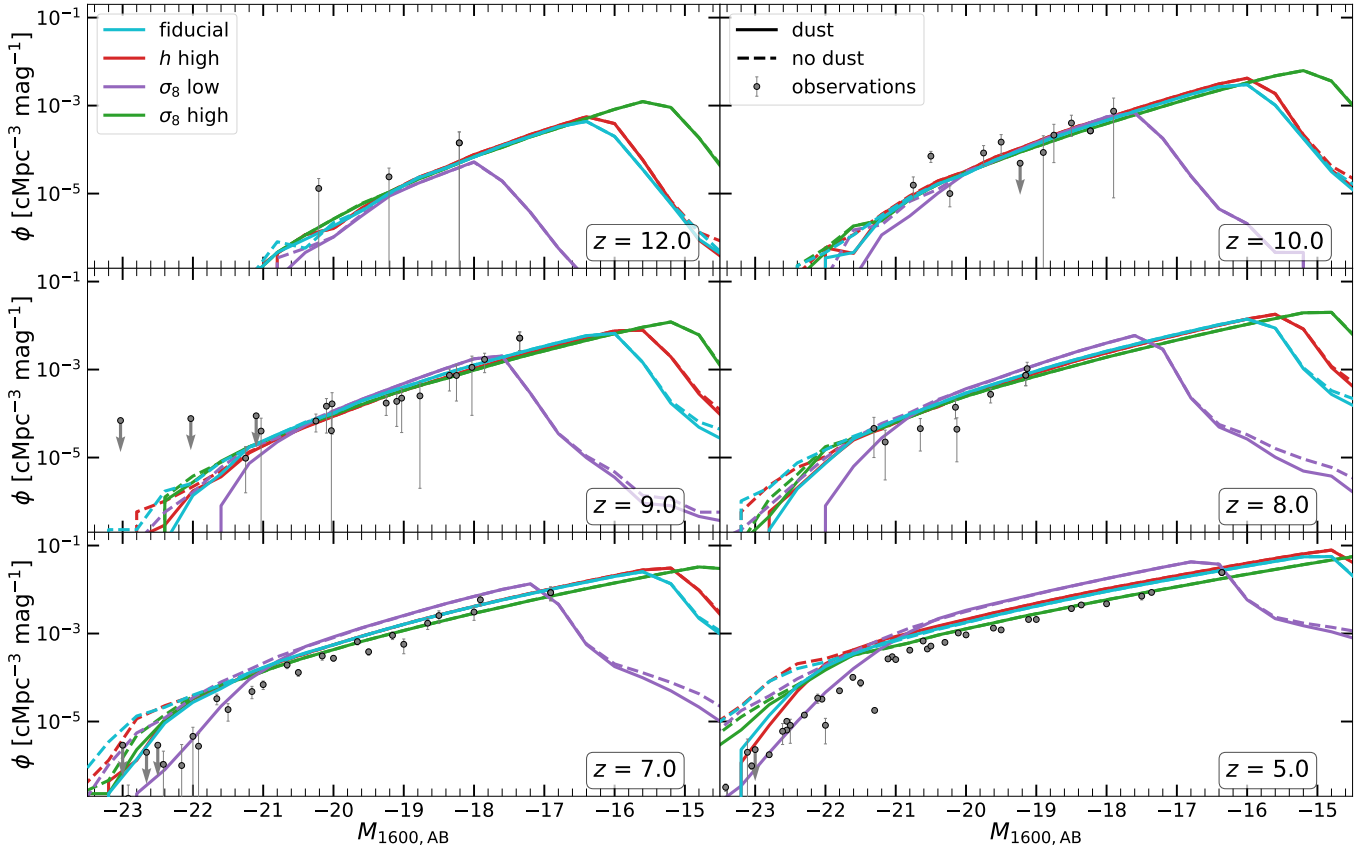


Figure A1: As Figure 2, but for the constrained case UVLFs at  $z = 12, 10, 9, 8, 7$  and  $5$ .

**APPENDIX B: MAPS OF  $\delta T_b$** 

In Figure B1, we show the maps of  $\delta T_b$  of the B-series middle slices (the simulations with “paired” initial conditions in the F&P pair of simulations) for the four cosmological models in the constrained case at  $z = 12, 10, 8,$  and  $6$  (from top to bottom). Here the darkest regions represent the ionized regions with  $\delta T_b = 0$ . Note that  $\delta T_b$  cannot assume negative values, due to the assumption of  $T_S \gg T_{\text{CMB}}$ . We note that the ionized regions of the A-series middle slices shown in Figure 3, correspond to the most neutral regions of Figure B1. This is because of the nature of the Fixed & Paired approach, as regions of matter clustering in the A-series should correspond to voids in the B-series by construction.

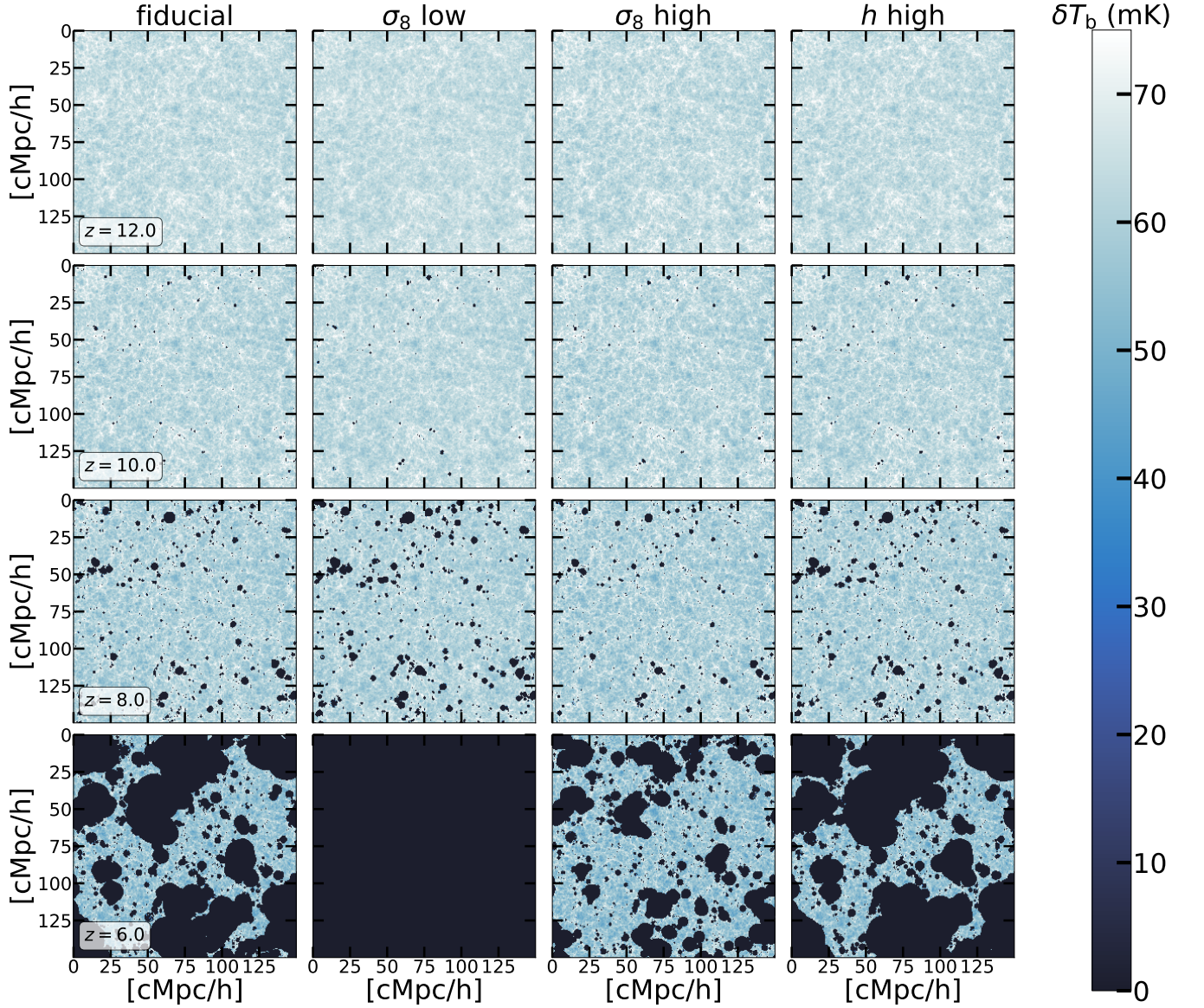


Figure B1: Same as Figure 3 but for the B-series of simulations.

**APPENDIX C: FIDUCIAL MODEL WITH  $f_{\text{esc}} = 25\%$** 

In Figure C1, we show the redshift evolution of the average of the A and B-series volume-averaged neutral hydrogen fraction  $\langle x_{\text{HI}} \rangle$  for an escape fraction of  $f_{\text{esc}} = 12.5\%$  (cyan) and  $25\%$  (brown). We note that as expected, doubling the escape fraction leads to a faster rate of reionization, getting 50% reionized by  $z \approx 7$  for  $f_{\text{esc}} = 25\%$  as compared to  $z \approx 6.4$  for  $f_{\text{esc}} = 12.5\%$ . However, both cases are in agreement with observations, except for redshifts  $z \leq 6$ , where the lower  $f_{\text{esc}}$  case has slightly higher values. Nevertheless, it is still within the margin of error of observations.

In Figure C2 we also show the redshift evolution of the normalized 21-cm signal power spectrum ( $\Delta_{21\text{cm}}^2$ ) at  $k = 0.15 \text{ hcMpc}^{-1}$ . We note that just like the other parameters as shown in Figure 8, the choice of  $f_{\text{esc}}$  impacts where  $\Delta_{21\text{cm}}^2 (k = 0.15 \text{ hcMpc}^{-1})$  peaks as well as its overall trend across redshift.

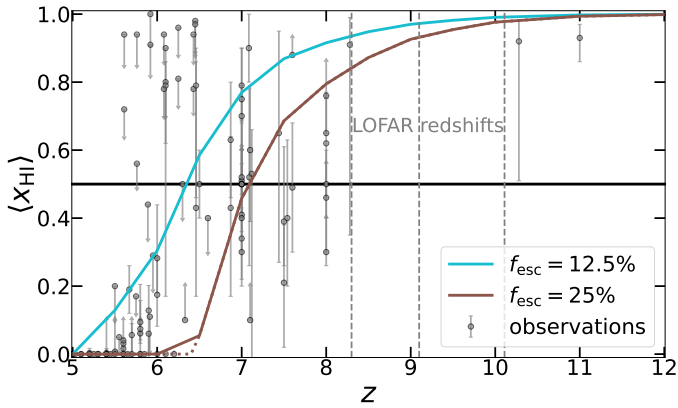


Figure C1: As Figure 4, but for the fiducial model, for an escape fraction of  $f_{\text{esc}} = 12.5\%$  (cyan) and  $25\%$  (brown).

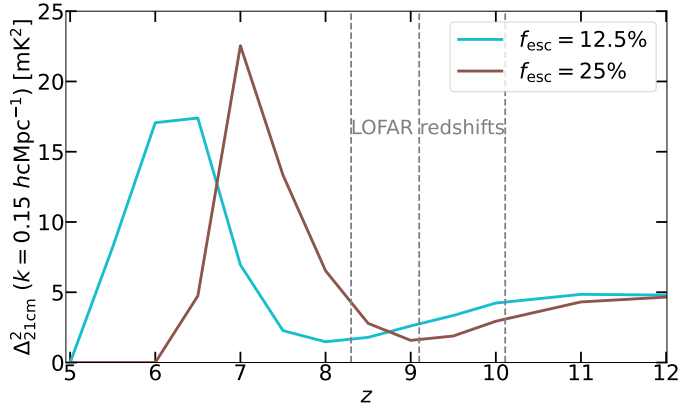


Figure C2: As Figure 8, but for the fiducial model, for an escape fraction of  $f_{\text{esc}} = 12.5\%$  (cyan) and  $25\%$  (brown).

This paper has been typeset from a  $\text{\TeX}/\text{\LaTeX}$  file prepared by the author.